Full-Field Optical Coherence Tomography and Monte Carlo Simulations for Biological Tissues

Phad Vaibhav Dnyandev

A Dissertation Submitted to
Indian Institute of Technology Hyderabad
In Partial Fulfillment of the Requirements for
The Degree of Master of Technology

भारतीय प्रौद्योगिकी संस्थान हैदराबाद
Indian Institute of Technology Hyderabad

Department of Biomedical Engineering

May, 2016

Declaration

I declare that this written submission represents my ideas in my own words, and where others' ideas or words have been included, I have adequately cited and referenced the original sources. I also declare that I have adhered to all principles of academic honesty and integrity and have not misrepresented or fabricated or falsified any idea/data/fact/source in my submission. I understand that any violation of the above will be a cause for disciplinary action by the Institute and can also evoke penal action from the sources that have thus not been properly cited, or from whom proper permission has not been taken when needed.

(Signature)

Phad Vaibhav Dnyandev

(– Student Name –)

BM14MTECH11006

(Roll No)

Approval Sheet

This thesis entitled “Full-Field Optical Coherence Tomography and Monte Carlo Simulations for Biological Tissues” by Phad Vaibhav Dnyandev is approved for the degree of Master of Technology from IIT Hyderabad.

Renu John
(Supervisor)

Harikrishnan
(Examiner 1)
Dr. Harikrishnan N. Unni

(Examiner 2)
Dr. V. KANCHANA

Acknowledgements

It is a privilege for me to write the following few lines in acknowledgement of those who helped me to complete the project work. I express my deepest gratitude to my thesis adviser Dr. Renu John, Head of the Department and Associate Professor, Department of Biomedical Engineering, Indian Institute of Technology Hyderabad for his valuable guidance and support during my project. His excellent guidance, invaluable suggestions and continuous encouragement boosted my moral towards the working of the project. His wide knowledge and logical way of thinking have been of great value for me.

I would also like to thank my class mates and PhD scholars for their assistance and support. It was a great pleasure for me to be a part of the Department of Biomedical engineering, IIT Hyderabad and I would like to thank all the faculty members for helping me in all stages of my work. The stay at IITH has been highly motivating for me personally as well as professionally and has inculcated in me numerous skills.

Finally, I would like to thank all my friends and family members for their continual support throughout the course of my studies.

Dedicated to

This little attempt is dedicated to all those who have technically made this world a better place to live in.

Abstract

Optical Coherence Tomography (OCT) is an emerging imaging technique that has been successfully demonstrated for non-invasive, non-contact and in-vivo imaging of biological specimen. Over the years, several OCT modifications have been developing so that present OCT system limitations can be overcome thereby extending its applications in various fields. Full-field OCT (FF-OCT) is one of the recent advancement in the OCT. In this thesis, FF-OCT system for imaging of biological tissues is presented. The image reconstruction of the system is performed using phase stepping methods to produce object images with better computational efficiency. This thesis also explores Monte Carlo method for mathematical modeling of light-tissue interaction. Monte Carlo is the statistical analysis of random sampling from the probability distributions used for tracking the photon movements inside the biological tissues. Various tissue models are created, and its fluence rates are analyzed. Furthermore, Monte Carlo method is developed for sampling and modeling of Gaussian beam on the multi-layered tissue. The absorption and fluence spectra have been analyzed for different types of Gaussian beam. Finally, comparison of beam profiles at different beam radius has been done.

Nomenclature

λ	Wavelength
K	Wave number
E_i	Electric field of incident wave
E_R	Electric field of reference beam
E_S	Electric field of sample beam
ΔL	Path length
l_c	Coherence length of the source
c	Speed of the light
n	Refractive index
Δx	Axial resolution
Δz	Lateral resolution
μ_a	Absorption coefficient
μ_s	Scattering coefficient
g	Anisotropy
φ	Phase
Ψ	Azimuthal angle
θ	Deflection angle
ξ	Random number
OCT	Optical coherence tomography
FF-OCT	Full field optical coherence tomography
N.A.	Numerical aperture
FF-OCM	Full field optical coherence microscopy
SLD	Superluminescent diode

List of Figures

Figure 2.1 Comparison of resolution and imaging depths of OCT to other imaging modalities 8

Figure 2.2 Basic configuration of Michelson interferometer 10

Figure 2.3 Schematic demonstrating the working of low coherence interferometry based on Michelson's interferometer........ 11

Figure 3.1 Experimental setup for full-field OCT by using Michelson geometry, SLD: Superluminescent diode, BS: beam-splitter, L: lens........ 17

Figure 3.2 Experimental setup for full-field OCT by using Linnik geometry18

Figure 3.3 Water absorption spectrum by considering different wavelengths 19

Figure 3.4 High and low NA focusing and the trade-off between the lateral resolution and depth of field 21

Figure 3.5 Original object before phase shift methods 24

Figure 3.6 Images at phase shifts (in rad) (A) 0 (B) π/2 (C) π........ 24

Figure 3.7 Reconstructed object after 3-step phase shift method........ 25

Figure 3.8 Images at phase shifts (in rad) (A) 0 (B) π/2 (C) π (D) 3π/2..... 26

Figure 3.9 Reconstructed object after 4-step phase shift method........ 27

Figure 4.1 Absorption spectra of biological tissues and absorption coefficients at some laser wavelengths. 32

Figure 4.2 A simple scattering event for understanding the angular dependence of scattering function. 32

Figure 4.3 A Cartesian coordinate system aligned for multilayered tissues.. 34

Figure 4.4 Flowchart for Monte Carlo simulation of multi-layered tissue.... 43

Figure 5.1 Skin tissue model 45

Figure 5.2 Probability density function of a Gaussian beam profile as per sampling rule A 48

Figure 5.3 Normalized intensity profile of a Gaussian beam profile as per sampling rule A 48

Figure 5.4 Probability density function of a Gaussian beam profile as per sampling rule B 49

Figure 5.5 Normalized intensity profile of a Gaussian beam profile as per sampling rule B 50

Figure 5.6 Collimated Gaussian beam for human skin 51

Figure 5.7 Fluence rate profile in ZX and ZY plane for collimated Gaussian beam 51

Figure 5.8 Focused Gaussian beam for human skin 52

Figure 5.9 Fluence rate profile in ZX and ZY plane for focused Gaussian beam 52

Figure 5.10 Similarities of fluence rate between flat-field beam and Gaussian beam is increasing as the beam size decreases 53

List of Tables

Table 5.1: Skin Tissue Parameters 46

Contents

Declaration ii

Approval Sheet iii

Acknowledgements iv

Abstract vi

Nomenclature vii

List of Figures viii

List of Tables x

1 Introduction 1

1.1 Motivation 1

1.2 Scope of the thesis 2

1.3 Organization of the thesis 3

2 Optical Coherence Tomography 6

2.1 History of OCT 6

2.2 Comparison with other imaging modalities 7

2.3 Variant types of OCT 8

2.4 Principles of OCT 9

2.4.1 Michelson's Interferometer 9

2.4.2 Low Coherence Interferometry 10

2.5 Light sources for OCT 11

2.6 OCT modifications 12

2.7 Applications of OCT 13

3 Full - Field OCT 16

3.1 Introduction 16

3.2 Features of FF-OCT 16

3.2.1 Basic Principle 16

3.2.2 Performances 18

3.2.3 Axial Resolution ... 19

3.2.4 Lateral Resolution ... 20

3.2.5 Depth of field ... 20

3.3 Noise Sensitivity ... 21

3.4 Reconstruction ... 23

3.4.1 3-step phase shift method ... 23

3.4.2 4-step phase shift method ... 25

4 Monte Carlo Modeling ... 29

4.1 Historical Review ... 29

4.2 Interaction of Light with Tissue ... 30

4.2.1 Introduction ... 30

4.2.2 Tissue Optical Properties ... 31

4.3 Description of Monte Carlo Simulation ... 33

4.3.1 The Coordinate Systems ... 33

4.3.2 Sampling of Random Variables ... 34

4.3.3 Photon Propagation Rules ... 36

4.3.3.1 Launching a photon packet ... 36

4.3.3.2 Step size of photon ... 37

4.3.3.3 Photon packet movement ... 38

4.3.3.4 Photon absorption ... 39

4.3.3.5 Photon scattering ... 39

4.3.3.6 Photon reflection or transmission at boundary ... 40

4.3.3.7 Photon reflection or transmission at interface ... 41

4.3.3.8 Termination of photon ... 42

5 Monte Carlo Simulations ... 45

5.1 Monte Carlo Tissue Model ... 45

5.2 Tissue Parameters ... 45

5.3 Monte Carlo modeling of a Gaussian Beams into Multi layered Tissue ... 46

5.3.1 General Characteristics of Gaussian Beams ... 46

5.3.2 Monte Carlo Sampling of a Gaussian Beam Profile ... 47

5.4 Monte Carlo Simulations of a different Gaussian Beam profiles 50
    5.4.1 Collimated Gaussian Beam 50
    5.4.2 Focused Gaussian Beam 51
5.5 Comparison of beam profiles at different beam radii 52

6 Summary and future work 56

References 58

Chapter 1

Introduction

1.1 Motivation

Optical imaging has been widely used in the diagnosis of the internal structure of human body. They have a wide variety of applications especially in the field of medicine, physics, material science and different areas of modern science. Since the introduction of Optical Coherence Tomography(OCT), it has been one of the most widely used methods for non-invasive imaging. OCT is based on the principle of low-coherence interferometry which utilizes Michelson interferometer as a basic geometry for imaging. OCT can image upto the depths of few millimeters into the sample with micron scale axial resolution. The object can be reconstructed in 3D by transversal scanning. In vivo cross sectional of tissue microstructures can also be done by using OCT. OCT is of main interest to the medical community because it provides tissue images at resolutions much better than other non-invasive 3D imaging modalities making it suitable for in vivo analysis at near histological resolutions. Nowadays various extensions of OCT have been developed which widen its application area but one of the main limitation of this technique is its small imaging depth which is due to multiple scattering.

There is necessity for the improvement of recent optical diagnostic techniques particularly OCT so that new methods for imaging can be developed for better understanding of light propagation inside biological tissues. The full-field OCT (FF-OCT) is one of the recent imaging advancement in OCT. In FF-OCT, we get the object image in *en face* orientation therefore scanning of light beam is not necessary. For its operation FF-OCT requires low coherence source is required thereby we prefer superluminescent diode (SLD) as an optical source. The final tomographic image retrieval is done by using CCD or CMOS camera.

For improvement of the effectiveness of modern diagnostic modalities and the development of new methods detailed study of light propagation in a tissue is essential. There is an absence of exact theoretical approach which can give correct description of light propagation in tissue. Numerical simulations can be a good approach for the solution of this problem. This approach gives flexibility to vary parameters for example, central wavelength, absorption coefficient, scattering coefficient, refractive index, coherence length, etc., which are difficult to manage in the experiment studies.

For simulations of light propagation in a tissue or any scattering media, a method for simulations should be properly chosen. Monte Carlo method is more suitable for light propagation inside the biological tissues and can be used for a wide range of analysis. The gist of this approach is that various calculations of random photon movements in the turbid media and further statistical analysis of the obtained data. Longer computational time is the main disadvantage of this method which can be overcome by efficient computational systems. The accuracy of the computational results is determined by verifying it with real experimental data.

1.2 Scope of the thesis

The primary objective of the thesis is the further development of OCT for the imaging of biological tissues. This is carried out by using a recently developed technique known as full-field OCT through which it is possible to capture an *en face* image directly. Computational image reconstruction is performed by phase stepping algorithms.

The secondary goal of the thesis is to understand light propagation inside the tissue by using Monte Carlo method. The tissue model under consideration is human skin. Sampling theory for the Gaussian beam has also been analyzed. Further the Gaussian beam profiles with various beam radius are compared.

1.3 Organization of the thesis

Chapter 2 of this thesis gives an overview of Optical Coherence Tomography. It gives a detailed comparison of OCT with existing imaging modalities, reviews different types of OCT, analyses the light source and most importantly discusses the basic principle of OCT. In the end the chapter gives potential applications, advantages, drawbacks and recent modifications of OCT.

Chapter 3 discusses the full-field OCT in depth. Key characteristics of FF-OCT are analyzed with reference to the SLD. Phase stepping method is applied for reconstruction. It also discusses the methods for adding phase for the given obtained image.

Chapter 4 gives detailed knowledge about Monte Carlo methods for biological tissues. The main tissue optical properties namely absorption coefficient, scattering coefficient, refractive index and anisotropy are analyzed with laser wavelengths. Monte Carlo based mathematical model is developed for further simulation. Photons propagation inside the tissue is discussed from launching of photon until its termination.

Chapter 5 shows the simulation results of the Monte Carlo approach on human skin model. Mathematical modeling of Gaussian beam is performed and new sampling method is derived. The absorption and fluence spectra are further analyzed for different types of Gaussian beam. At last, comparison of beam profiles at different beam radius is done.

Chapter 6 gives the summary and future work for the given project.

Chapter 2

Optical Coherence Tomography

2.1 History of OCT

The first OCT was demonstrated by Huang et al. in the year 1991 [1]. It was mainly used to study the eye for evaluating any imperfections in the eye tissue layers [2]. Later commercial OCT systems were developed and widely accepted by ophthalmologists.

The basic OCT systems are based on a moving reference mirror but they suffered limitations in the scanning speed. There is a need to change the position of reference mirror to obtain intensities of backscattered light from different depths in the given biological sample. This particular technique is known as Time domain OCT (TD-OCT). Further several advances have been developed which increase axial resolution [3] and achieve good speed of scanning [4].

The main reason for the improvement in axial resolution was mainly due to the introduction of broadband light sources into the OCT systems [5]. Frequency domain approach increases the data acquisition speed due to simultaneous collection of backscattered light from all tissue depths in a single A-scan without the movement of the reference mirror. The two frequency domain techniques are Spectral domain OCT (SD-OCT) and Swept Source OCT (SS-OCT). In SD-OCT broadband light source spectrometer along with a CCD camera is used while as in

SS-OCT a narrow bandwidth source swept through a broad range of frequencies and a photodetector is used. Signal to Noise Ratio (SNR) is improved due to the implementation of these techniques. Computational image reconstruction provides the 3D volumetric tissue imaging.

2.2 Comparison with other imaging modalities

To understand OCT imaging, it is helpful to compare it with related medical imaging techniques [6]. Different parameters such as resolution, imaging depth, image acquisition time, complexity, etc. are used to compare various imaging modalities. Figure 2.1 shows a comparison of resolution and imaging depths of OCT to other imaging modalities and clearly depicts where OCT stands in terms of resolution and imaging depth. OCT has imaging depth limited to a few millimeters which is less compared to ultrasound and standard clinical imaging modalities but has a better resolution. For ultrasound imaging, the resolution is mainly dependent on the sound wave frequency and it is approximately 0.1 to 1 mm. These typical frequencies have been chosen because of absorption spectra for a biomedical tissue as it will give good depth for imaging inside the human body. Nowadays, ultrasound is using high frequencies for various medical applications. Intravascular imaging is one of the popular examples of it. Resolutions of 15–20 μm and finer have been attained with frequencies approximately equal to 100MHz. For ultrasound, main limitation for imaging is the selection of frequencies. If we go for high frequencies it will give less depth due to absorption parameters in biological tissue. For attaining high resolution one can prefer microscopy techniques such as confocal microscopy.

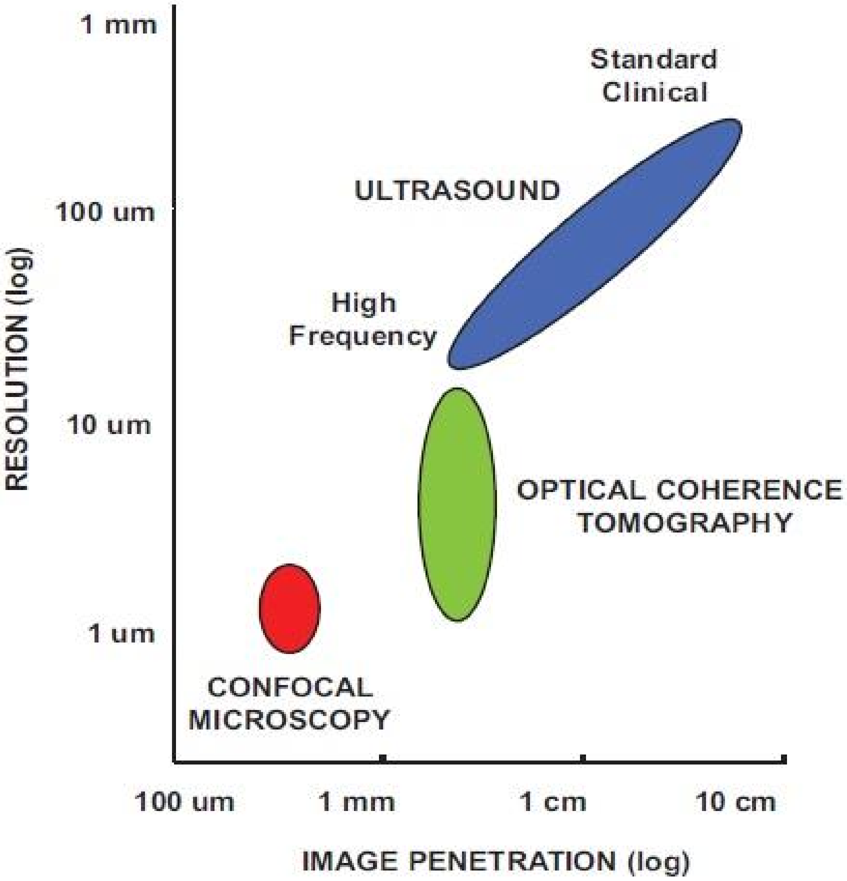

Figure 2.1: Comparison of resolution and imaging depths of OCT to other imaging modalities [6]

OCT is often compared with confocal microscopy which has an extremely high resolution but confocal tomography is not suitable for applications where a depth of penetration is the main criteria. Hence, OCT fills the gap between confocal microscopy and ultrasound imaging. OCT is good in terms of a resolution but lags image penetration due to strong scattering.

2.3 Variant types of OCT

The main types of OCT are the time domain optical coherence technology (i.e. TD-OCT) and the frequency domain optical coherence technology (FD-OCT). The basic principle to acquire an image in time domain OCT is to scan the reference arm mirror for matching the optical path from the reflections of the sample which is kept at another arm. Further, the time domain OCT can be classified into three types namely, point scan OCT, linear OCT or line field OCT and full-field OCT. The key difference of FD-OCT from TD-OCT is that the reference mirror is kept stationary. In a single depth scan all the reflected light from different depths in the tissue is recorded simultaneously. There are two different techniques used in FD-OCT namely Spectral Domain OCT (SD-OCT) and Swept source OCT (SS-OCT). The SD-OCT utilizes a spectrometer to analyze the output of the interferometer and the spectral interferogram is then recorded on the camera. The SS-OCT makes use of a frequency tunable laser, which is rapidly swept across a range of frequencies for each sample location and then recorded on a photodetector. Intensity as a function of wavelength is recorded in both the techniques. Fourier domain analysis is performed on this acquired data but the signal to noise ratio in frequency domain OCT is superior to time domain OCT [7].

However, frequency domain OCT also has its own drawbacks. Frequency domain OCT suffers from one main limitation which is the double spectral symmetry. The optical spectrum which we get at the output consists of symmetrical terms. Different methods are tried to overcome this fundamental problem. Phase shifting interferometry [8] is one the technique which can overcome this issue. Post processing takes a lot of time in frequency domain OCT and also frequency domain sampling rate deteriorates time domain signal quality. In time domain OCT, dynamic focusing is used to get a better lateral resolution which cannot be used in frequency domain OCT.

2.4 Principles of OCT

2.4.1 Michelson's Interferometer

The most common interferometer configuration employed in OCT systems is Michelson interferometer illustrated in Fig. 2.2. The incident light source is divided into two beams E_R and E_S. E_R is travelling through the reference arm while as E_S is travelling through the sample arm. Both the beams travel different distances in the two arms of the interferometer. The electric field due to the interference of the two beams is $E_R + E_S$. The intensity measured by a detector is proportional to the square of the total field and is given as:

$$I_0 \sim |E_R|^2 + |E_s|^2 + 2E_R E_S \cos(2k\Delta L) \qquad 2.1$$

Where, ΔL is the path length mismatch between the beams in the sample and the reference arm. Interference fringes are generated with the scanning movement of a reference arm.

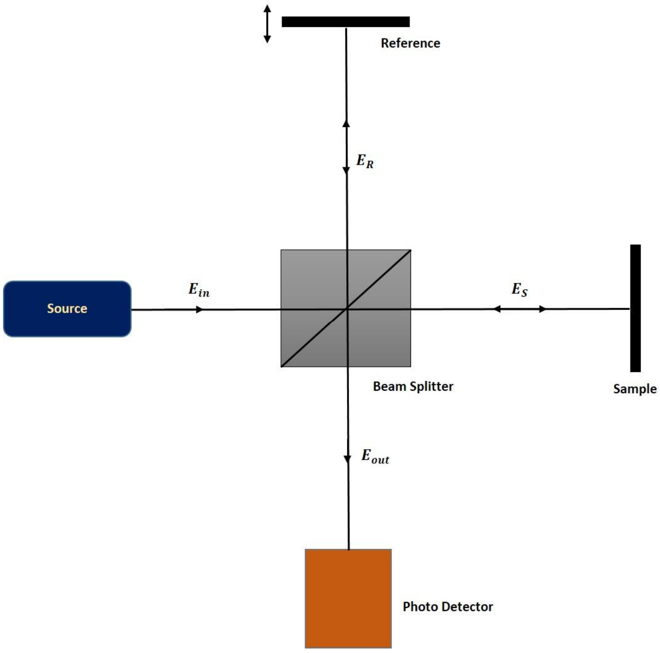

Figure 2.2: Basic configuration of Michelson interferometer

2.4.2 Low Coherence Interferometry

For detections of an echo time delay a very high time resolution is required. To measure distances with submicron resolution femtosecond time resolution is necessary. Due to the time scale limits we cannot use direct electronic means of detection. Hence, alternative measurement methods like Low-Coherence Interferometry must be explored [9]. Low-Coherence Interferometry technique measures the magnitude and echo time delay of the backscattered light with very high sensitivity. Interferometry techniques perform correlation or interference between backscattered light from the tissue and light that has travelled a known distance or time delay through a reference path. In the case of coherence light, interference will be observed over a wide range of path length differences. A low-coherence light source is necessary to detect optical echoes. Coherence length is the key characteristic for low-coherence light and coherence length is inversely proportional to the bandwidth of the light. For observing interference pattern the path lengths of the reference and sample arms are matched to the coherence length light generated by given light source. The magnitude and echo time delay of light can be measured by scanning the reference arm and demodulating the interference signal. The modulation of the interference signal can be effectively used to determine the magnitude and echo time delay of light.

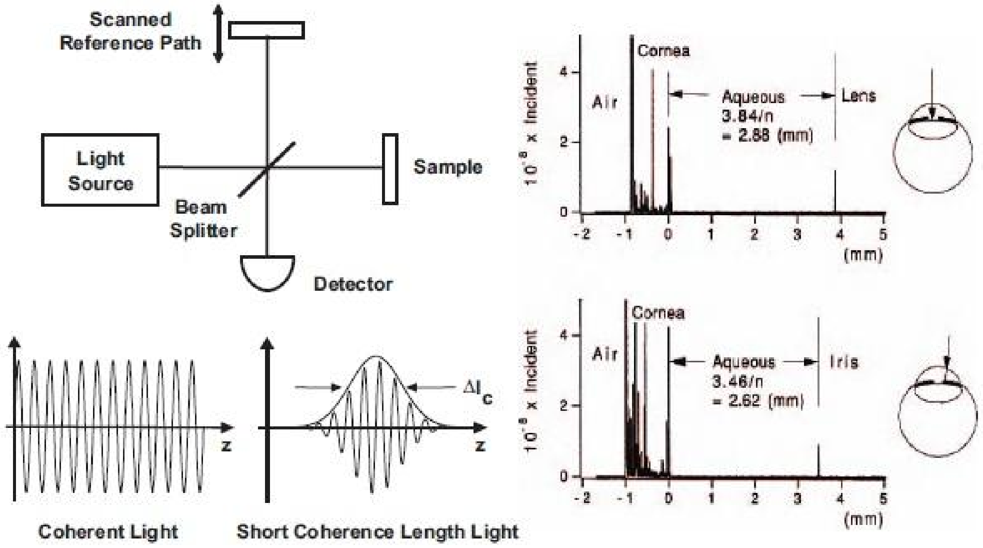

Scanned Reference Path
Light Source
Beam Splitter
Sample
Detector
Coherent Light
Short Coherence Length Light
z
z
Δl_c
10^{-8} x Incident
Air
Cornea
Aqueous
3.84/n
= 2.88 (mm)
Lens
Air
Cornea
Aqueous
3.46/n
= 2.62 (mm)
Iris
-2
-1
0
1
2
3
4
5
(mm)

Figure 2.3: Schematic demonstrating the working of low coherence interferometry based on Michelson's interferometer [6]

2.5 Light sources for OCT

As per several theoretical and experimental studies, the light source is one of the main parameters for OCT system. The common requirements of sources for OCT imaging are emission in the near infrared, short temporal coherence length and high irradiance. Considering this requirement superluminescent diodes or femtosecond lasers are usually used as low-coherent light sources for OCT setups.

Femtosecond lasers compared to SLD provides higher resolution due to its narrower coherence function shape as the axial resolution of the OCT system is inversely proportional to the source spectrum width. Because of a high price of Femtosecond lasers, the SLDs are more frequently used in OCT systems especially for commercial models employed in medical application areas. Nowadays, the coupling of several SLDs with close central wavelengths is developed which allows us to obtain longitudinal resolution close to that given by femtosecond lasers.

2.6 OCT modifications

Basic characteristics of OCT are improved due to the magnificent improvement in the basic OCT setup. There are several advances in the OCT which add new extensions and widen the area of its usage. These new methodologies are spectroscopic, polarization sensitive, polarization diversity, and Doppler flow imaging.

Spectroscopic information about the tissue is extracted by using spectroscopic OCT. This information is achieved by the interferometric signal which is useful for mapping out the spectral absorption and backscattering properties of molecules in the tissue. Polarization sensitive OCT finds out the changes in polarization state of the light. The major reason for this change is the anisotropic properties of the tissue. The obtained information in polarized sensitive OCT is used for mapping the functional and structural variability in the tissue. Doppler imaging is used for blood flow analysis in blood vessel. Basic principle beyond Doppler imaging is a Doppler shift in backscattered light which can be detected by the Fourier transformation of the interference signal. A relatively recent extension of OCT which images the distribution of magnetic molecular agents in tissue specimen is called Magnetomotive OCT (MM-OCT). It has the capability to detect nanometer scale displacements hence it is preferred for finding biomechanical tissue parameters. Other recent developments are the ultra-high speed OCT (UHS-OCT) and polarization-sensitive OCT (PS-OCT). In the USH-OCT the scanning mirror is replaced by a stable mirror such that the error due to the mechanical movement of the mirror is almost reduced which leads to the improvement of SNR. For the PS-OCT, radiation of the source is polarized which increases the imaging depth which was limited by multiple scattering. The recent developments in the OCT technology have thus enabled newer applications.

2.7 Applications of OCT

Nowadays OCT and its extensions are broadly used for biomedical imaging and structural understanding of objects under investigation. The very first clinical application of OCT was in the imagery of eye due to its ease of being a transparent tissue. It has helped the medical community to diagnose and monitor eye diseases. Longer wavelengths are being used because of their better penetration depth. The main reason for choosing longer wavelengths is to avoid optical scattering. OCT can detect early stage of cancers through identification of early neoplastic changes in the tissue [10]. Many in vitro studies have investigated OCT's ability to diagnose early cancers in several tissues such as gastrointestinal, respiratory, urinary and gynecology [11].

OCT can guide surgical interventions because of its ability to view subsurface features of tissue in vivo [12]. OCT can be integrated with surgical microscopes or can be used as a handheld probes for surgeries. OCT can be easily integrated with existing medical imaging modalities thereby leading its usage in multimodal imaging [13]. OCT is also important for industrial quality control applications. OCT is applied for diagnostics of various materials for example polymer matrix materials and paper. OCT is can also be applied for nondestructive evaluation of highly scattering polymer-matrix composites to estimate residual porosity, fibre architecture and structural integrity. Recently OCT was recognized to be valuable for evaluation of old objects of arts and archaeological artefacts thus allowing to avoid their destruction.

In addition to above discussed applications over the years, OCT has also been applied for the development of highly advanced high-density optical data storage systems. OCT mainly serves as a reading device for such data storages as OCT is capable of fast scanning which allows it to take a reading from a complex 3D structure such as multilayer optical disc which provides the possibility to design data storages that have properties that exceed the ones in modern models.

Chapter 3

Full - Field OCT

3.1 Introduction

Optical coherence tomography (OCT) has drastically improved since its invention. In time domain OCT, the image is acquired by scanning reference arm and laser source whereas in frequency domain OCT, scanning of the reference arm is replaced by the spectrometric scan. We cannot get the 2D image directly in time domain OCT and frequency domain OCT but FF-OCT can acquire a 2D image at a particular depth over a transverse scan which we called as the *en face* image. In full-field OCT the entire field of the image is illuminated with low spatial coherence light as compared to conventional OCT [14]. FF-OCT also reduces the complexity in the setup as well as in the reconstruction algorithms. *En face* imaging is a prominent biological technique as compared to other imaging modalities such as confocal microscopy, ophthalmoscopes and fundus cameras. The major applications of *en face* imaging are in eye, skin and other various tissues [15].

3.2 Features of FF-OCT

3.2.1 Basic Principle

Full-field OCT is based on the principle of low coherence interferometry. Low coherence light source is mainly used in the basic setup and SLD is used as a light source in the experimental setup. Optical isolator is used after SLD to prevent it from damage. After SLD light is collimated by using lens (L1). At first step, basic

Michelson geometry [16] is implemented for capturing the object image. The camera is used for the acquisition of 2D en face image of the object. Figure 3.1 explains basic experimental setup for full field OCT.

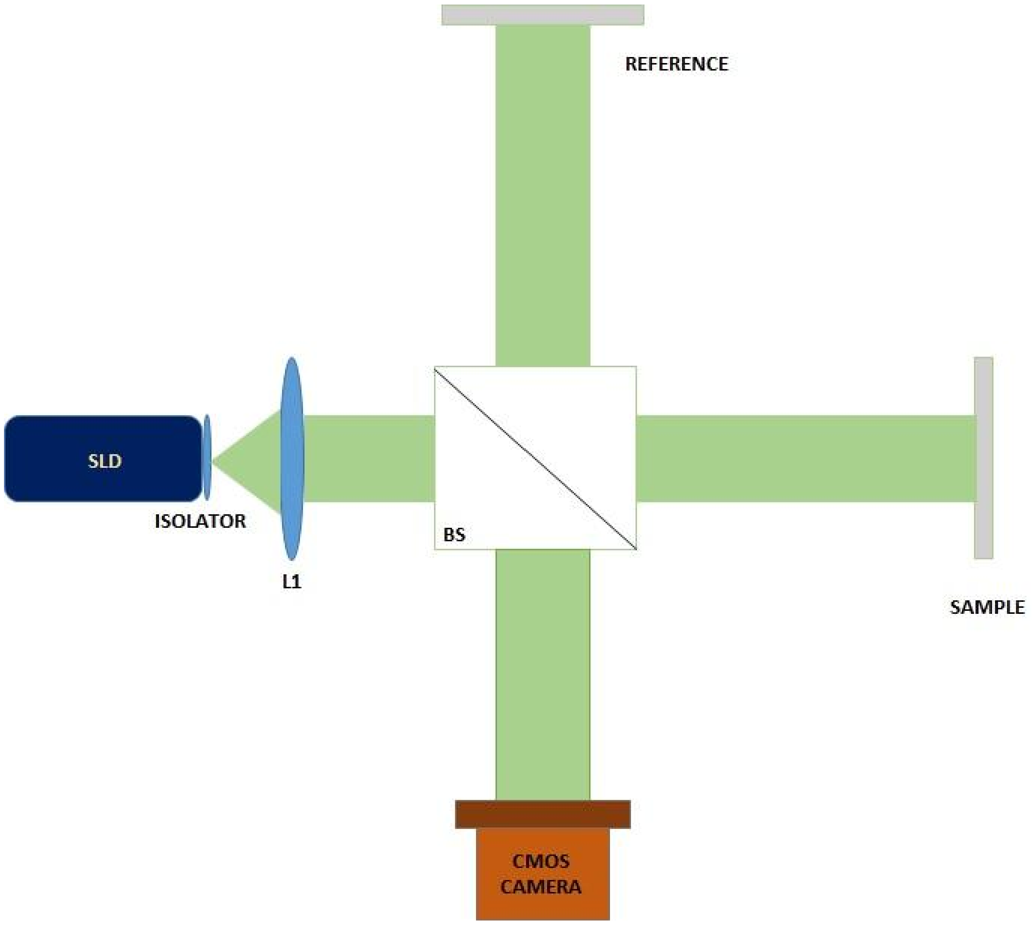

Figure 3.1: Experimental setup for full-field OCT by using Michelson geometry, SLD: Superluminescent diode, BS: beam-splitter, L: lens

Two identical microscopic objects are placed in the two arms of the interferometer which extend the setup geometry to Linnik type [17]. High spatial resolution can be obtained in Linnik configuration as we can adjust the numerical aperture. The basic experimental setup for FF-OCT by using Linnik interferometry configuration is given in Fig. 3.2.

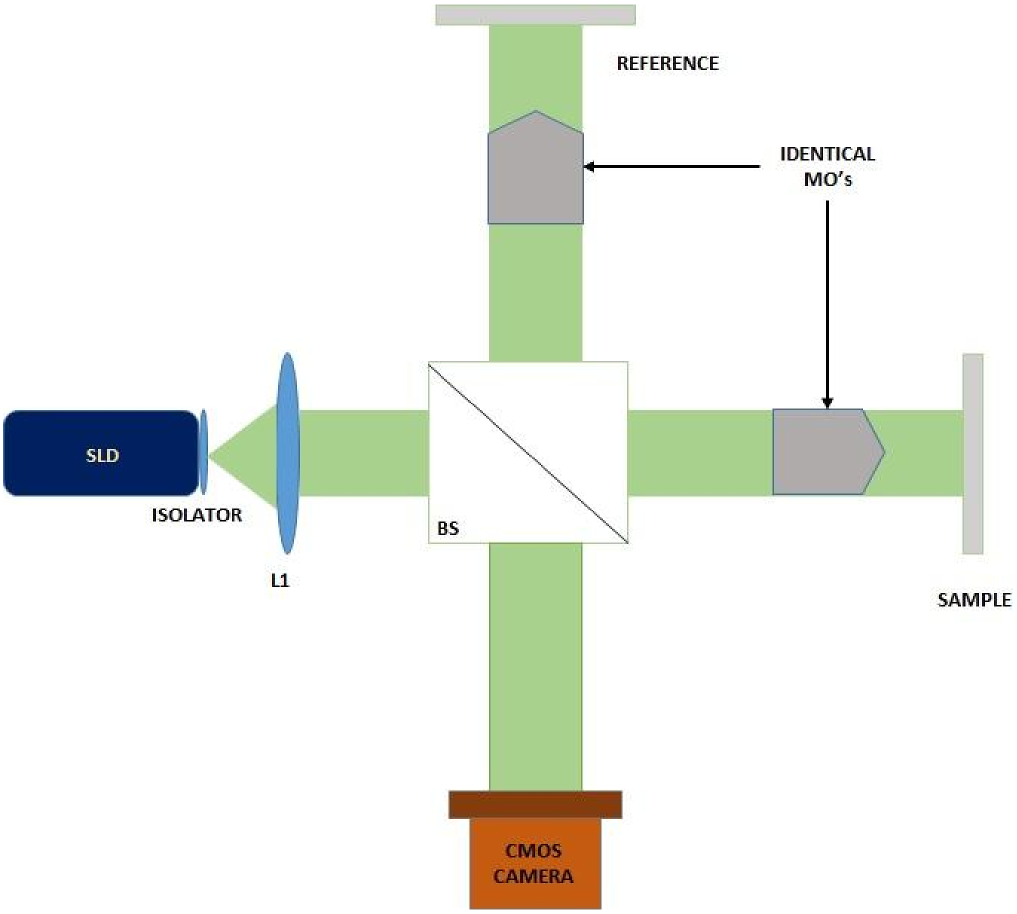

Figure 3.2: Experimental setup for full-field OCT by using Linnik geometry

3.2.2 Performances

The optical source characteristics are the key parameters for the general performance of the FF-OCT. In the case of axial resolution coherence length plays a vital role and in the case of lateral resolution wavelength is important as it determines the depth of the field [18]. The line width $\Delta\lambda$ of the source and the coherence length l_c of the source are inversely proportional. For choosing a light source for OCT, the most important parameters are wavelength and bandwidth of it. Along with these two parameters, single-transverse mode power and stability are of critical important. The depth of penetration inside tissue is limited due to scattering and absorption. Absorption in the biological tissue is mainly due to water because water is the basic constituent in every tissue. Absorption again depends on wavelength of the source therefore the local minimum region is identified based on wavelength which we defined as absorption window. This region is in the range of 650 nm to 1400 nm. As per Fig. 3.3, there is a window with lower absorption termed “therapeutic windows” for biomedical imaging which is in between 600nm to 800 nm. Numerous analytical, theoretical and experimental studies have been done for this window therefore selection of wavelength is very important in OCT [16].

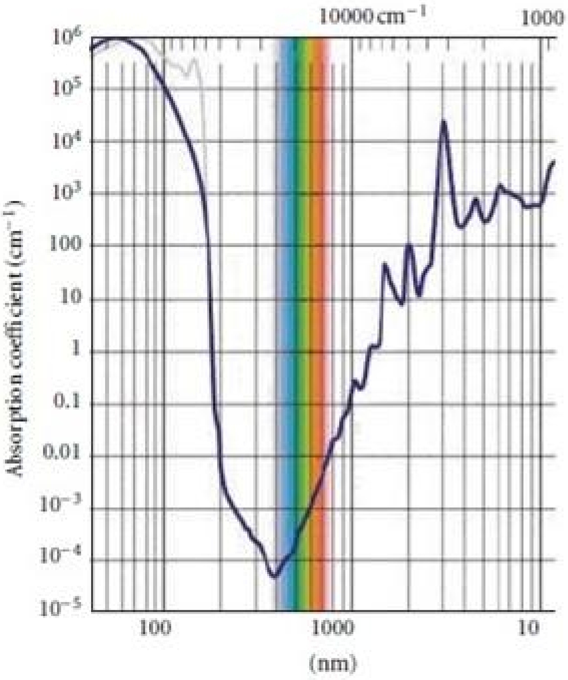

Figure 3.3: Water absorption spectrum by considering different wavelengths [19]

3.2.3 Axial Resolution

As compared to conventional microscopy, axial resolution and lateral resolution are decoupled from each other. Image quality is mainly governed by the axial resolution of the optical imaging system [20]. OCT is capable of providing axial submicron level resolutions and it is not dependent on the beam focusing and spot size. OCT measurement is based on low coherence interferometry. So, the width of the autocorrelation function determines the axial resolution and it is inversely proportional to the bandwidth of the light source. For a Gaussian spectrum, the axial resolution is given by,

$$\Delta z = \frac{l_c}{2} = \frac{2\ln 2}{\pi}\frac{c}{\Delta\nu} = \frac{2\ln 2}{\pi}\frac{\lambda^2}{\Delta\lambda} \cong 0.44\ \frac{{\lambda_0}^2}{\Delta\lambda} \qquad 3.1$$

In the above equation, Δz is the FWHM (Full Width at Half Maximum) of the autocorrelation function, $\Delta\lambda$ is the FWHM of the source power spectrum and λ_0 is the source center wavelength. Because of this inverse relationship between the axial resolution and source bandwidth the high axial resolution is achieved by using broad-bandwidth light sources [21]. The most common light source currently used in OCT systems is superluminescent diode (SLD). SLD used in the given optical setup has a bandwidth $\Delta\lambda = 43.3$ nm, which corresponds to a coherence length of 9 µm.

3.2.4 Lateral Resolution

The lateral resolution in OCT is mainly calculated by the diffraction limited spot size of the focused beam similar to that in optical microscopy [22]. The diffraction limited spot size is inversely proportional to the NA (Numerical Aperture) or focusing angle of the beam [23]. The lateral resolution Δx can be given by,

$$\Delta x = \frac{4\lambda}{\pi}\left(\frac{f}{d}\right) = \left(\frac{2\lambda}{\pi}\right)\frac{1}{NA} \qquad 3.2$$

In the above equation, f is the focal length of the objective lens and d is the $\frac{1}{e^2}$ Gaussian beam waist.

3.2.5 Depth of field

From the Eq. (3.2), we can note that by using a large numerical aperture the beam can be focused to a small spot size and this can be used to achieve fine lateral resolution but at the same time lateral resolution is also related to the depth of field. The imaging depth of field or confocal parameter b, is $2z_R$, or two times the Rayleigh range:

$$2\Delta z_R = b = \frac{\pi \Delta x^2}{2\lambda} \tag{3.3}$$

So, there is a trade-off between transverse resolution and depth of field as increase in transverse resolution causes a decrease in depth of field. Figure 3.4 shows two cases of using low NA and high NA focusing and their corresponding field depth. Usually, low NA focusing is performed in OCT systems to obtain a large depth of field. The confocal parameter b, in this case, is larger than the coherence length. However, low NA leads to larger focused spot sizes and hence low lateral resolution. OCT can also be performed with high NA focusing in order to obtain high lateral resolutions but it reduces the depth of field to a large extent.

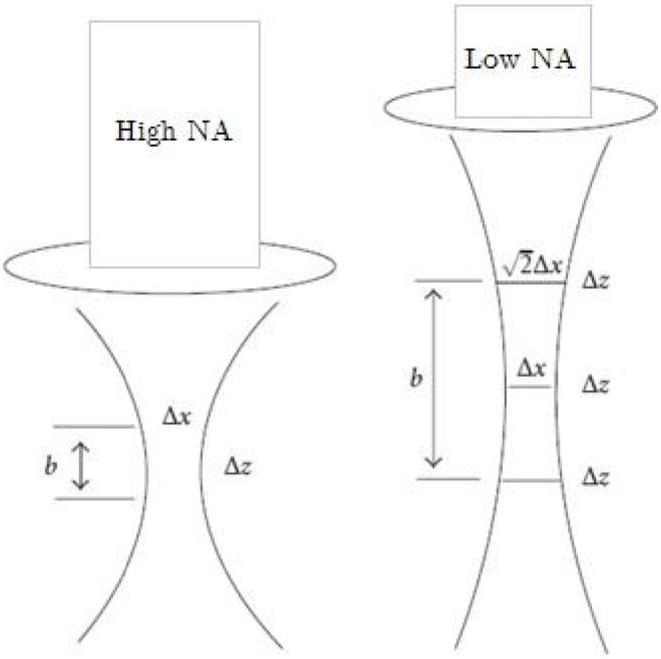

Figure 3.4: High and low NA focusing and the trade-off between the lateral resolution and depth of field

3.3 Noise Sensitivity

The sensitivity of an OCT system is determined by signal to noise ratio of the given system. It is defined as the ratio of signal power generated to the noise power. It is given by the following equation:

$$SNR = \frac{{I_S}^2}{{I_N}^2} \qquad 3.4$$

In the above equation, I_S is the photocurrent captured at the detector end. This photocurrent can be defined mathematically as,

$$I_S = \frac{\eta\, q_e}{h\, \omega_0}\, P \qquad 3.5$$

Where, η is the quantum efficiency of the detector, q_e and h are the constant quantities namely electron charge and planks constant. ω_0 is the angular frequency and P is the integral of the source power spectral density. I_N is the overall noise of the optical detection system which consists three important sources namely shot noise (I_{SH}), relative intensity noise (I_{RIN}), and thermal noise (I_{TH}). Hence, the total noise current is the contribution of all three noise sources and it is given as,

$${I_N}^2 = {I_{SH}}^2 + {I_{RIN}}^2 + {I_{TH}}^2 \qquad 3.6$$

The shot noise is prominent compared to other noise parameters. If we compare other noise parameters compared to shot noise they are very negligible. So, we consider shot noise as a main contributing parameter.

Therefore, we can express the total noise as:

$$I_N = I_{SH} = \sqrt{2 q_e I_{DC} B} \qquad 3.7$$

In the above equation, I_{DC} is the DC photo current and B is the detection bandwidth. So, considering the DC photo current for this shot noise limit we can simplify further,

$$I_N = \sqrt{\frac{\eta\, q_e}{h\omega_0}\, 2PB} \qquad 3.8$$

Therefore, by substituting (3.5) and (3.8) into (3.4) gives,

$$SNR = \frac{\eta P}{2h\omega_0 B} \qquad 3.9$$

Normally, the SNR is also called as a figure of merit when it is expressed in logarithm form and is related to the power SNR by,

$$SNR = 10\ \log\left(\frac{\eta P}{2h\omega_0 B}\right) \qquad 3.10$$

From the above equation, we can conclude that higher source power is required to maintain the SNR performance of the system [16].

3.4 Reconstruction

The cross sectional image is acquired at different depth in OCT. The image acquired by camera can be mathematically [24] represented by,

$$I(x,y) = I_0(x,y) + A_i(x,y)\sin\emptyset(x,y) \qquad 3.11$$

This equation is mainly divided into three parts: (1) I_0(x, y) represents the background image, (2) A_i(x, y) represents the tomographic image of the i^{th} layer and (3) sin Φ(x, y) represents the interference fringes. Phase steeping algorithm is used for retrieving the tomographic image.

3.4.1 3-step phase shift method

The acquired image by camera is represented mathematically. So, this mathematical equation can be solved to get the tomographic image. The original image is simulated computationally and it is shown in the below figure,

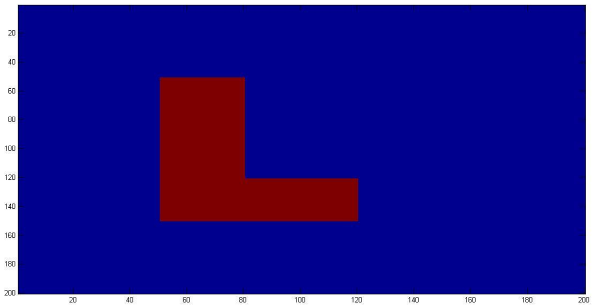

Figure 3.5: Original object before phase shift methods

Now we consider original image without any phase shift i.e. image with zero phase shift. After grabbing two $\pi/2$ images and solving it with the original image, the resultant tomographic image is given by:

$$A_i(x,y) = \{[I_1(x,y) - I_0(x,y)]^2 + [I_1(x,y) - I_0(x,y)]^2\}^{1/2} \qquad 3.12$$

This above equation can be more generalized if we go with an angle φ instead of $\pi/2$. Now by considering φ as a phase angle the mathematical expression for tomographic image is:

$$A_i(x,y) = \{[I_1(x,y) - I_0(x,y)]^2 + [\big(I_2(x,y) - I_0(x,y)\big) - \big(I_1(x,y) - I_0(x,y)\big)\frac{\cos\varphi}{\sin\varphi}]^2\}^{1/2} \qquad 3.13$$

We have considered φ is equal to $\pi/2$ for simulations. The three images after adding $\pi/2$ as a phase are given as in below figure,

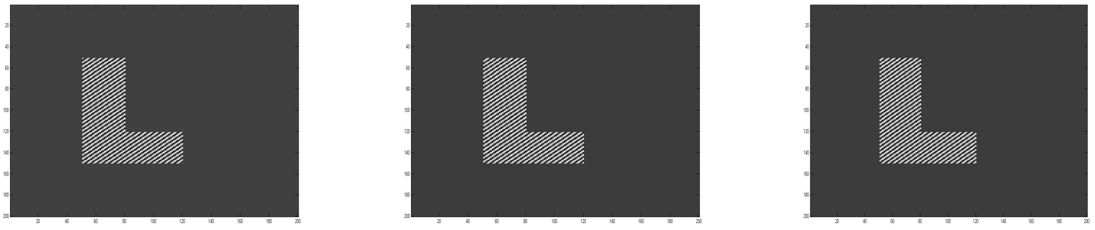

(A) (B) (C)

Figure 3.6: Images at phase shifts (in rad) (A) 0 (B) π/2 (C) π

The reconstructed tomographic image is obtained by the above equations. The reconstructed image is given as:

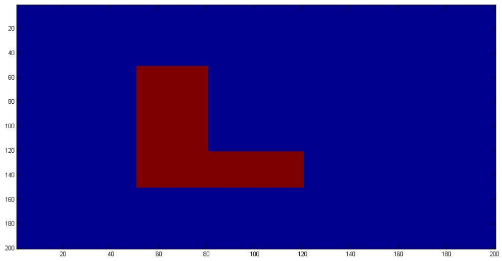

Figure 3.7: Reconstructed object after 3-step phase shift method

Though we get reconstructed object but this method has major drawback with its phase. Here, we have to add known phase value. The arbitrary phase cannot be obtained at last, so there is a need to take more images to overcome this disadvantage. So, we prefer adding more phase shifts rather than going with three phase shifts.

3.4.2 4-step phase shift method

In the 4-step phase shifting method [25] the original image is acquired by giving zero phase. The obtained image by the camera can be represented as the zero phase image. Same object which is considered for three step is considered for four step algorithm.

Now, there is a need to add constant phase at regular interval to solve the phase stepping equation for reconstruction. All four equations are represented mathematically as following:

$$\begin{aligned} I_1(x,y) &= I_0(x,y) + A_i(x,y)\cos[\emptyset(x,y) - 3\varphi] \\ I_2(x,y) &= I_0(x,y) + A_i(x,y)\cos[\emptyset(x,y) - \varphi] \\ I_3(x,y) &= I_0(x,y) + A_i(x,y)\cos[\emptyset(x,y) + \varphi] \\ I_4(x,y) &= I_0(x,y) + A_i(x,y)\cos[\emptyset(x,y) + 3\varphi] \qquad 3.14 \end{aligned}$$

In the above equations Φ is a constant phase angle, and 2φ is the phase shift added to each step. We have considered phase amount equals to π/2 at each step. The four images at four phases results as:

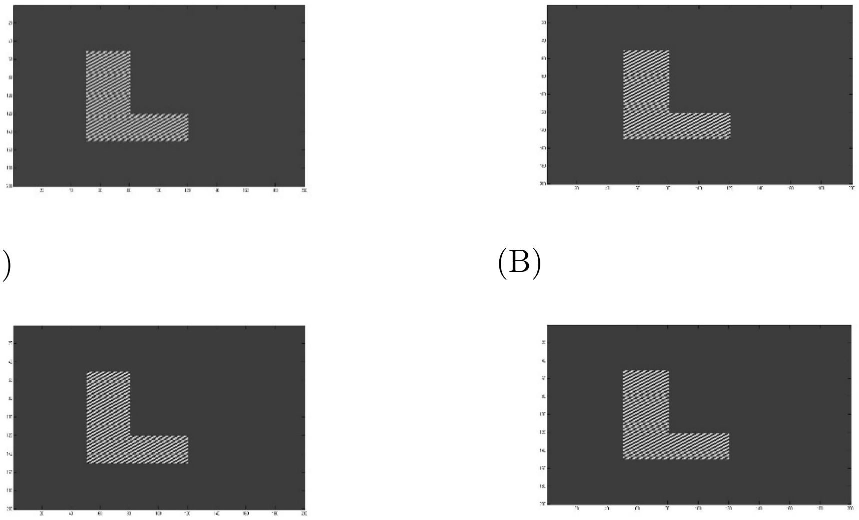

(A) (B)

(C) (D)

Figure 3.8: Images at phase shifts (in rad) (A) 0 (B) π/2 (C) π (D) 3π/2

The tomographic image can be obtained by solving these four equations simultaneously. After solving we get:

$$A(x,y) = \left[\left(\frac{I_1(x,y) - I_4(x,y) + I_2(x,y) - I_3(x,y)}{8\sin\varphi\cos^2\varphi}\right)^2\right] + \left[\left(\frac{I_1(x,y) + I_4(x,y) - I_2(x,y) - I_4(x,y)}{8\sin\varphi\cos^2\varphi}\right)^2\right]^{1/2} \qquad 3.144$$

$$\tan\varphi = \left\{\frac{3[I_2(x,y) - I_3(x,y)] - [I_1(x,y) - I_4(x,y)]}{I_1(x,y) - I_4(x,y) + I_2(x,y) - I_3(x,y)}\right\}^{1/2} \qquad 3.155$$

So the final reconstructed tomographic image is given as,

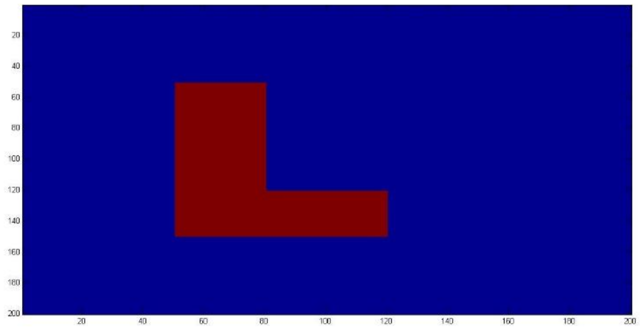

Figure 3.9: Reconstructed object after 4-step phase shift method

Chapter 4

Monte Carlo Modeling

4.1 Historical Review

Laser is an acroymn for "Light Amplification by Stimulated Emission of Radiation" in which light is emitted based on the principle of optical amplification. The basic principle behind it is the simulated emission of photons. The laser light has a very high degree of temporal coherence and spatial coherence which cannot be achieved using other sources. The laser beam can be focused to tiny spot which gives high irradiance. As per the applications, there are different types of the lasers such as a chemical laser, femtosecond laser, He-Ne laser, metol-vapour laser, dye laser, gas laser etc. The majority of potential applications of lasers are in medical treatments such as skin disorders, orthopedics, gynecology, neuroscience, optogenetics etc. The depth of penetration inside a biological sample depends on the tissue optical properties mainly scattering coefficient, absorption coefficient, anisotropy, refractive index etc. The tissue optical properties vary according to the wavelength.

For tissue interaction with the laser light we treat it as an scattering and absorption medium [26]. With changing the optical properties photon absorption can cause heating which leads to ionization. Selection of laser for any medical treatment is mainly decided by its beam power, irradiation time and spot size. For modeling of any type of laser treatment, it is essential to examine the distribution of photon in the tissue [27].

An exact evaluation of laser propagation in tissue requires a model that describes the spatial distribution of photons inside tissue with their absorbing properties, scattering properties and refractive indices. This is excellently done by Monte Carlo simulation. Monte Carlo simulations are matched with transport theory which is an analytical theory for describing light propagation in turbid media like tissue. Monte Carlo methods can handle almost every light source, detector and tissue optical properties [28]. A Large number of photons are launched at a location defined by Cartesian coordinates. The path of photons is tracked by the direction cosines of given coordinates. For calculating the random distance, random sampling is essential. Random sampling of photon step size, azimuthal angle and scattering angle is done in Monte Carlo method. Random number is generated computationally which follows the uniform profile. The weight of the photon is tracked after each step. Loss of photon weight is mainly due to absorption and scattering. Finally, absorption spectra are plotted and fluence rate is determined [29].

4.2 Interaction of Light with Tissue

4.2.1 Introduction

As per the particle theory of light, light is a steams of photons. Particle theory elucidates the quantum nature of light. The interaction of light mainly depends on tissue optical properties and the properties of incident light [30]. While travelling through tissue light may follow the same path or change its direction. During light interaction with the tissue, photons may get absorbed or remain unabsorbed within the tissue. The unabsorbed light either gets transmitted to the other layer. It may get reflected from the tissue surface as well.

Reflection occurs when the light interacts with the front of tissue or scatters and passes through the tissue interface while leaving the tissue. Scattering of light occurs when there is fluctuation in the refractive indices. It leads to change the direction without changing the wavelength. Tissue optical parameters play a vital role in this process [31].

4.2.2 Tissue Optical Properties

The optical characteristics of the biological tissues are the refractive index, the absorption coefficient, the scattering coefficient and anisotropy factor. The refractive index is defined as the ratio of the speed of light in a vacuum to its speed in the medium. Hence, the refractive index is resistance for light during its propagation inside its tissue. When light incident on the interface between two layers with different refractive indices, a fraction of incident light suffers from the specular reflectance and remaining fraction of light will be transmitted as per Snell's law [32].

Absorption of photons by biological tissue is very important for therapeutic as well as diagnostic study [33]. The absorption coefficient is defined as the probability of absorption per unit path length whereas the scattering coefficient is defined as the probability of photon scattering per unit path length of travelling photon. The summation of absorption and scattering coefficient gives the total attenuation coefficient which can be defined as the probability of photon interaction per unit infinitesimal path length [34]. Scattering manly cause due to small variation in the in the refractive indices. The absorption coefficients at some typical laser wavelengths are shown in Fig.4.1. Typical biological tissues have considered for the analysis of absorption coefficient and wavelength.

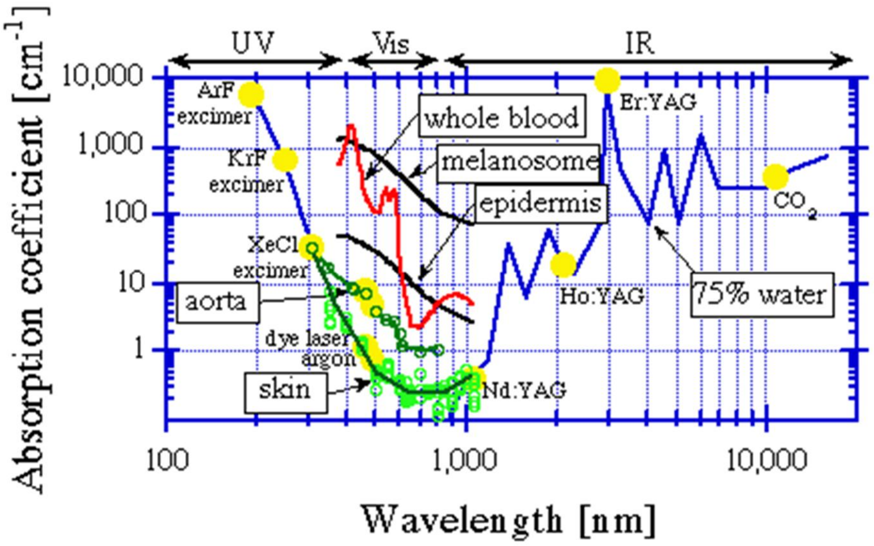

Figure 4.1: Absorption spectra of biological tissues and absorption coefficients at some laser wavelengths [35]

Anisotropy is defined as the average cosine of the deflection angle at a single scattering event. The angular dependence of scattering is called as a scattering function. Figure 4.2 gives the clear view about the scattering and its angular dependence.

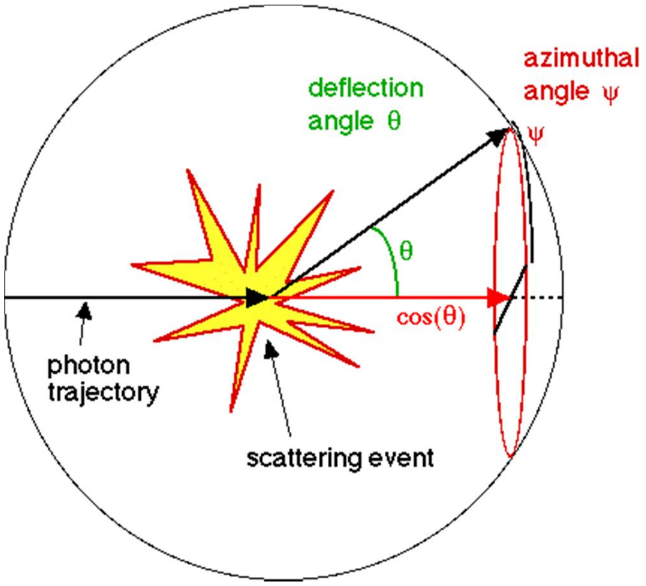
deflection angle θ
azimuthal angle ψ
ψ
θ
cos(θ)
photon trajectory
scattering event

Figure 4.2: A simple scattering event for understanding the angular dependence of scattering function [36]

The scattering function is defined as the probability of photon scattering per unit solid angle. For isotropic scattering, anisotropy is zero which leads propagation in the forward direction.

4.3 Description of Monte Carlo Simulation

4.3.1 The Coordinate Systems

The Monte Carlo simulation deals with the transport of an infinitely narrow photon beam perpendicularly incident on a multi-layered tissue. Each layer can be considered as infinite in length described by the thickness and tissue optical properties which is discussed earlier. There is the necessity of another two parameters refractive indices of top and bottom medium. The main parameters for simulation are photon absorption, photon fluence rate, reflectance and transmittance. The photon absorption and the photon fluence rate are correlated. They can be converted back and forth by using the local absorption coefficient of the tissue. Reflectance and transmittance at the top and bottom surface are also calculated.

Monte Carlo simulations consider all three coordinate systems simultaneously. A Cartesian coordinate system is mainly used for tracking photon packets. The origin of the coordinate system is the photon incident point on the tissue surface as given in the Fig. 4.3. A cylindrical coordinate system is used to update internal photon absorption. The Cartesian coordinate system as well as the cylindrical coordinate system share the origin and the z axis. A moving spherical coordinate system is used for sampling the propagation direction. The deflection angle and azimuthal angle are sampled in the spherical coordinate system. Finally, the photon direction is updated in terms of the directional cosines in the Cartesian coordinate system [37].

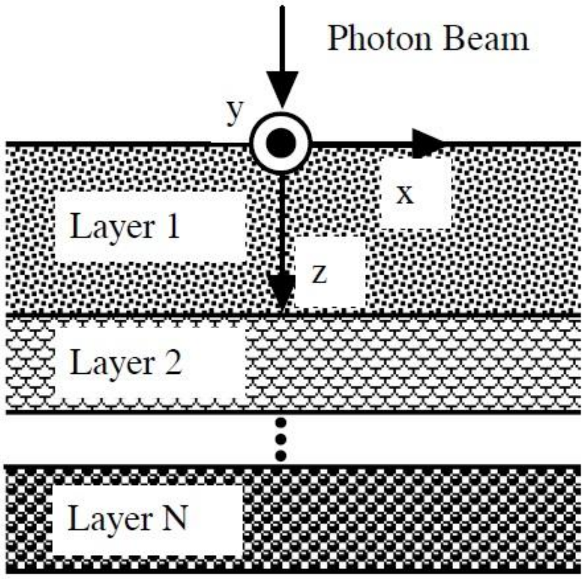

Figure 4.3: A Cartesian coordinate system aligned for multilayered tissues [38]

4.3.2 Sampling of Random Variables

Random sampling of variables from the well-defined probability distributions is done in the Monte Carlo simulations. Here we consider a random variable X, which is needed for the Monte Carlo simulation of photon propagation in tissue. The distribution of X over the interval (a, b) is defined by a probability density function (i.e. pdf). The probability density function is normalized such as:

$$\int_a^b p(X)dX = 1 \tag{4.1}$$

The value of X can be generated as a pseudo-random number generator. This pseudo-random number generator provides a random variable ξ which is having uniformly distribution over (0, 1). The cumulative distribution function for this uniformly distributed random variable can be given as:

$$F(\xi) = \begin{matrix} 0 & if\ \xi \leq 0 \\ \xi & if\ 0 < \xi \leq 1 \\ 1 & if\ \xi > 1 \end{matrix} \tag{4.2}$$

There is necessity mapping between ξ and X because ξ lies in the (0, 1) and X lies in (a, b), so, the variable X and variable ξ have a one-to-one mapping. This ultimately leads to the following results:

$$P\{f(0) < X \leq f(\xi_1)\} = P\{0 < \xi \leq \xi_1\} \qquad 4.3$$

Above equation can also be written as:

$$P\{a < X \leq X_1\} = P\{0 < \xi \leq \xi_1\} \qquad 4.4$$

As per the definition of cumulative distribution functions, above equation can be written as:

$$F_X(X_1) = F_\xi(\xi_1) \qquad 4.5$$

This cumulative distribution function can be updated in terms of the probability density function which can be given as:

$$\int_a^{x_1} p(X)dX = \xi_1 \qquad 4.6$$

Which can be further solved as:

$$\int_a^{x_1} p(X)dX = 1 - \xi_1 \qquad 4.7$$

(1 – ξ1) and ξ1 can be interchanged, as both have the same distribution.

Now, the sampling of the step size for photon movement is to be discussed fully in subsequent points. The probability density function for photon step size is given:

$$p(s) = \mu_t \, e^{-\mu_t s} \qquad 4.8$$

In the above equation s is the photon step size and μ_t is the interaction coefficient. This above probability density function can be solved to get sample value, based on random number ξ.

$$\xi = \int_0^{s_1} p(s)ds = \int_0^{s_1} \mu_t \, e^{-\mu_t s} \, ds = 1 - e^{\mu_t s} \qquad 4.9$$

Which leads to;

$$s_1 = \frac{-\ln(1-\xi)}{\mu_t} \quad 4.10$$

The above expression is equivalent to:

$$s_1 = \frac{-\ln(\xi)}{\mu_t} \quad 4.11$$

So to get the final sample value, there is the necessity of probability distribution. Once we know the probability distribution we can calculate probability density function [38]. This probability density function is useful for random sampling which can be correlated with cumulative distribution function. The cumulative distribution function gives the final sample value [36].

4.3.3 Photon Propagation Rules

4.3.3.1. Launching a photon packet

As per implicit photon capture many photons travel as a packet along a particular pathway are equivalently propagated. Photons are propagated as a packet and are assigned a certain weight W. The photon is injected orthogonally into the tissue at the origin.

Cartesian coordinates are used to denote the current position of the photon. Photon direction is updated by direction cosines, which are given as:

$$\mu_x = r.x$$

$$\mu_y = r.y$$

$$\mu_z = r.z \quad 4.12$$

In the above equation, μ_x, μ_y, μ_z are direction cosines in the x, y and z directions respectively. Initial photon position is (0, 0, 0) whereas the direction cosines are set to (0, 0, 1). This Cartesian coordinate system for tracking photon movement is much simpler than cylindrical coordinate system.

After launching the photon, there may be chances of the mismatched boundary at the tissue surface, so some specular reflectance may occur. The specular reflectance can be given as,

$$R_{sp} = \frac{(n_1 - n_2)^2}{(n_1 + n_2)^2} \qquad 4.13$$

In the above equation, n_1 and n_2 are refractive indices of the outside medium and tissue respectively.

If the first layer is glass, then there are chances of multiple reflection and transmissions. The refractive index for glass layer can be taken as n_3. The specular reflectance (R_{sp}) is then computed by:

$$R_{sp} = r_{1+} \frac{r_2(1 - r_1)^2}{(1 - r_1 r_2)} \qquad 4.14$$

In the above equation, r_1 and r_2 are the Fresnel reflectance's of the glass layer. The glass layer is on the top of the tissue surface. The Fresnel reflectances for this layer are given as,

$$r_1 = \frac{(n_1 - n_2)^2}{(n_1 + n_2)^2} \qquad 4.15$$

$$r_2 = \frac{(n_3 - n_2)^2}{(n_3 + n_2)^2} \qquad 4.16$$

Above equations are not strictly correct; they may be very good estimates of the real specular reflectance for thick tissues [34]. The photon weight is reduced due to specular reflectance which is updated as,

$$W = 1 - R_{sp} \qquad 4.17$$

4.3.3.2. Step size of photon

For calculating photon step size, a sampling of probability distribution function is necessary, so first we need to calculate the photon's step size. It is calculated from the basic definition of interaction coefficient. According to the basic definition of interaction coefficient μ_t, the probability of interaction per unit path length is:

$$\mu_t = \frac{-dP\{s \geq s'\}}{P\{s \geq s'\}ds'} \qquad 4.18$$

Which can be solved as,

$$d(\ln(P\{s \geq s'\})) = \mu_t ds' \qquad 4.19$$

After integrating above equation, we get:

$$p(s \geq s_1) = e^{-\mu_t s_1} \qquad 4.20$$

Which can also be written as:

$$p(s < s_1) = 1 - e^{-\mu_t s_1} \qquad 4.21$$

This probability distribution is solved with the help of cumulative distribution function which gives:

$$s_1 = \frac{-\ln(1-\xi)}{\mu_t} \qquad 4.22$$

Which is similar to,

$$s_1 = \frac{-\ln(\xi)}{\mu_t} \qquad 4.23$$

The total step size is given by the following probability function:

$$P\{s \geq s_{sum}\} = e^{(-\sum_i \mu_{ti} s_i)} \qquad 4.24$$

In the above equation, i is an index to a layer, μ_{ti} is the interaction coefficient and s_i is the step size for respective layer. The total step size s_{sum} can be written as:

$$s_{sum} = \sum_i s_i \qquad 4.25$$

Considering above equation, the relation between step size and random number can be given as:

$$\sum_i \mu_{ti} s_i = -\ln(\xi) \qquad 4.26$$

Above equation clearly indicates that the sampling can be expressed as the total dimensionless step size.

4.3.3.3. Photon packet movement

After step size s, the photon is moved in the tissue. The coordinates of photons are updates as per the step size and directional cosines [40]. The previous coordinates are considered to keep track of photon. The position of the photon packet can be given as:

$$x \leftarrow x + \mu_x s$$
$$y \leftarrow y + \mu_y s$$
$$z \leftarrow z + \mu_z s \qquad 4.27$$

Left hand side variable have the new values, and the variables on the right hand side have the old values.

4.3.3.4. Photon absorption

After launching photon inside the tissue, photon weight decreased due to the absorption. This absorption at that site is calculated by considering absorption coefficient. Some amount of photon's weight is deposited in the local grid. This deposited weight (ΔW) of photon is calculated by:

$$\Delta W = W \frac{\mu_a}{\mu_t} \qquad 4.28$$

There should be the track of photon's weight. So it is updated as:

$$W \leftarrow W - \Delta W \qquad 4.29$$

4.3.3.5. Photon scattering

After photon absorption, its weight is decremented. So there may be chances of photon scattering. It is necessary for statistical sampling of the deflection angle and an azimuthal angle. The Henyey-Greenstein function [41–43] is for a sampling of the deflection angle. The Henyey-Greenstein function is given as:

$$p(\cos\theta) = \frac{1 - g^2}{2(1 + g^2 - 2g\cos\theta)^{3/2}} \qquad 4.30$$

In the above equation, g is the anisotropy of a given turbid media and has a value between −1 and 1. For isotropic scattering, the value of g is equal to 0 and for forward scattering is almost 1. For biological tissues, the value of g is in between 0.3 and 0.98. The value of $cos\theta$ is given as following:

$$\cos\theta = \begin{cases} \frac{1}{2g}\left\{1+g^2-\left[\frac{1-g^2}{1-g+2g\xi}\right]^2\right\} & if\ g>0 \\ 2\xi-1 & if\ g=0 \end{cases} \quad 4.31$$

Now, the azimuthal angle Ψ is sampled as:

$$\Psi = 2\pi\xi \quad 4.32$$

After sampling of deflection and azimuthal angle, the direction cosines are given as,

$$\mu'_x = \frac{\sin\theta}{\sqrt{1-\mu_z^2}}\left(\mu_x\mu_z\cos\Psi - \mu_y\sin\Psi\right) + \mu_x\cos\theta$$

$$\mu'_y = \frac{\sin\theta}{\sqrt{1-\mu_z^2}}\left(\mu_y\mu_z\cos\Psi + \mu_x\sin\Psi\right) + \mu_y\cos\theta$$

$$\mu'_z = -\sin\theta\cos\Psi\sqrt{1-\mu_z^2} + \mu_z\cos\theta \quad 4.33$$

For small angle of photon packet, the direction cosines are approximated as:

$$\mu'_x = \sin\theta\cos\Psi$$

$$\mu'_y = \sin\theta\sin\Psi$$

$$\mu'_z = SIGN(\mu_z)\cos\theta \quad 4.34$$

μ_z is positive, when SIGN(μ_z) is equal to 1 and when μ_z is negative when SIGN(μ_z) is equal to -1.

4.3.3.6. Photon reflection or transmission at boundary

For handling reflection or transmission at tissue-tissue or air-tissue interface we should know the exact step size. This can be solved by considering minimal step size. This step size is again dependent on the value of direction cosine in the z direction. For μ_z less than zero, it is given as,

$$s_s = \frac{(z-z_0)}{\mu_z} \quad 4.35$$

Otherwise, it is given as,

$$s_s = \frac{(z-z_1)}{\mu_z} \quad 4.36$$

The upper and lower boundaries of the current layer for a photon is given by z respective z coordinates, z_0 and z_1 respectively. The remaining step size has to be updated as well. Now the angle of incidence is calculated as,

$$\alpha_i = \cos^{-1}(|\mu_z|) \tag{4.37}$$

For calculating the angle of reflectance, Snell's law is used. The refractive indices of the incident and transmitted layer are n_i and n_t respectively. So, as per the Snell's law,

$$n_i \sin \alpha_i = n_t \sin \alpha_t \tag{4.38}$$

Fresnel's formula is used for calculating internal reflectance, which is expressed as:

$$R(\alpha_i) = \frac{1}{2}\left[\frac{\sin^2(a_i - a_t)}{\sin^2(a_i + a_t)} + \frac{\tan^2(a_i - a_t)}{\tan^2(a_i + a_t)}\right] \tag{4.39}$$

Finally, a random number is used for determining the internal reflectance. If $\xi \leq R(\alpha_i)$, then the photon is internally reflected otherwise it escape from the tissue [44]. The direction cosines are updated as per the reflection or transmission.

4.3.3.7. Photon reflection or transmission at interface

Photon step may cross several layers of tissue if a photon step size is large enough to hit a tissue-tissue interface. If the photon packet is transmitted to the next layer of tissue, it should propagate in the next layer. For propagating in the next layer, it should have a defined step size. So, the remaining step size for the new layer is given by:

$$s \leftarrow \frac{s\ \mu_{t1}}{\mu_{t2}} \tag{4.40}$$

In the above equation, μ_{t1} and μ_{t2} are the interaction coefficients for tissue 1 and tissue 2 respectively. The direction cosines are again updated and the step size is again checked [45]. The process is repeated until the photon step size is small enough to fit in one layer.

4.3.3.8. Termination of photon

Photon termination can happen naturally as it undergoes several reflections or transmissions. But beyond a certain threshold, photon packet contains very minute information. So, going for further propagation will increase computational time and these photon packets are not useful as they contain very little information. Proper termination should be followed which can follow conservation of energy. There is an excellent technique used for the same purpose called as roulette [46, 47]. This is based on chances for survival thereby it gives some chances to survive for the last photon packet. If photon packet is unable to survive then the photon packet is decremented to zero and the termination of photon packet has done. The detailed flowchart of the whole process is shown in the Fig. 4.4.

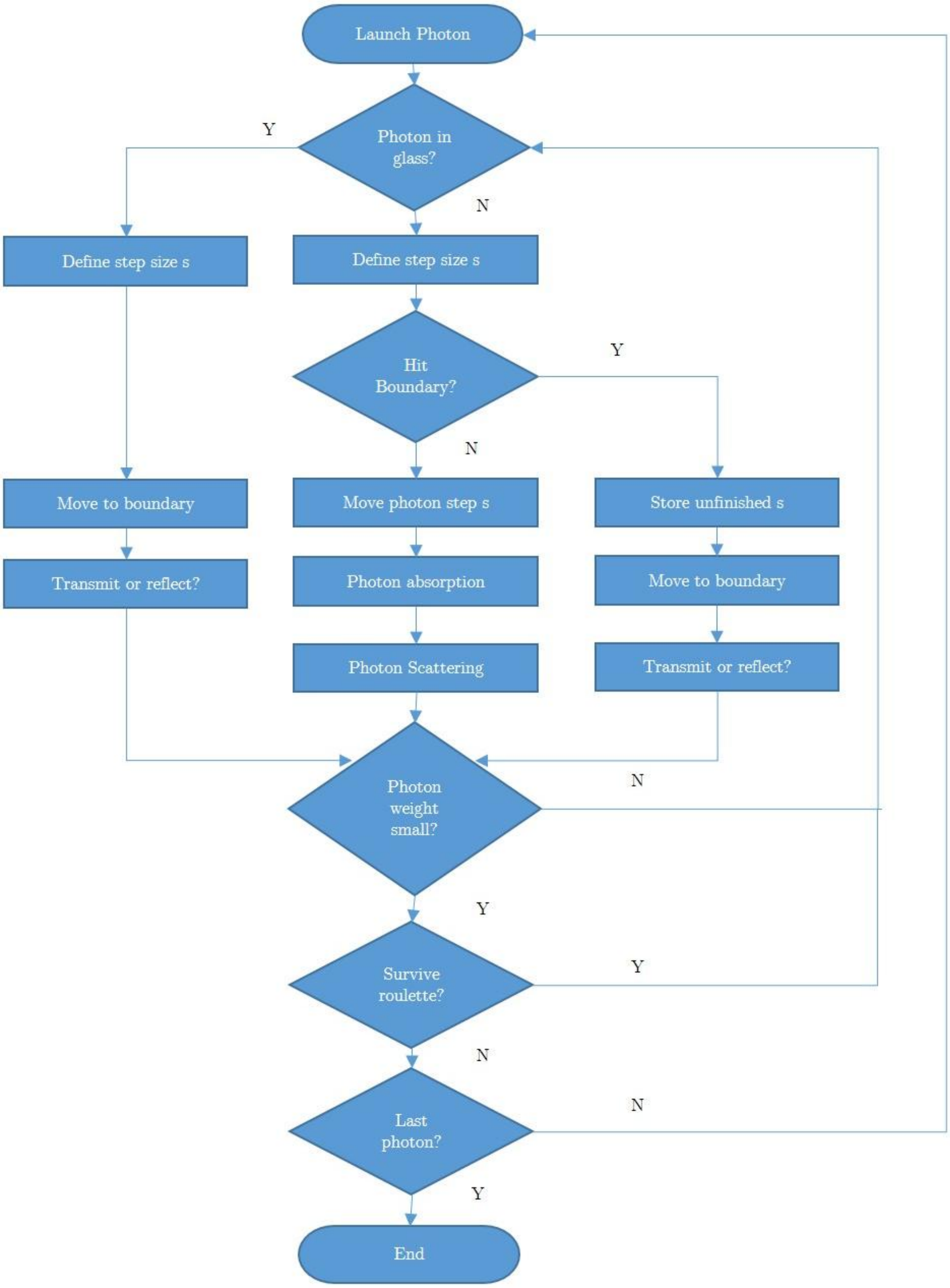
Launch Photon
Photon in glass?
Y
N
Define step size s
Define step size s
Hit Boundary?
Y
N
Move to boundary
Move photon step s
Store unfinished s
Transmit or reflect?
Photon absorption
Move to boundary
Photon Scattering
Transmit or reflect?
Photon weight small?
N
Y
Survive roulette?
Y
N
Last photon?
N
Y
End

Figure 4.4: Flowchart for Monte Carlo simulation of multi-layered tissue

Chapter 5

Monte Carlo Simulations

5.1 Monte Carlo Tissue Model

The geometrical model considered for simulation consists of two main layers of the skin namely dermis and epidermis, the blood vessel is also embedded into it. The simulated tissue model is shown in the Fig. 5.1.

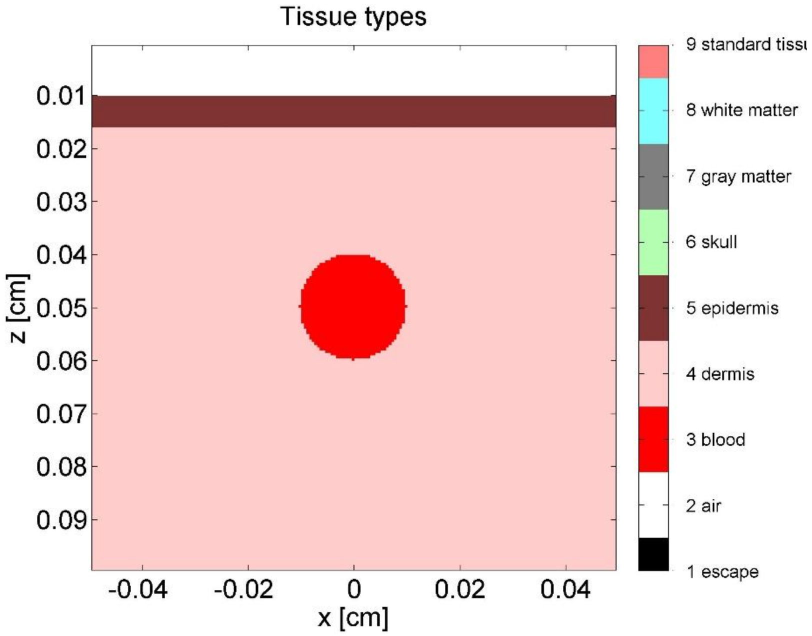
Tissue types
z [cm]
0.01
0.02
0.03
0.04
0.05
0.06
0.07
0.08
0.09
x [cm]
-0.04
-0.02
0
0.02
0.04
9 standard tissu
8 white matter
7 gray matter
6 skull
5 epidermis
4 dermis
3 blood
2 air
1 escape

Figure 5.1: Skin tissue model

5.2 Tissue Parameters

The tissue parameters considered here are absorption coefficient, scattering coefficient, anisotropy and total interaction coefficient. They are listed below:

Table 5.1: Skin Tissue Parameters

Sr.No.	Type	μ_a	μ_s	G
1	Escape	0.0001	1.0	1.000
2	Air	0.0010	10.0	1.000
3	Blood	230.5427	94.0	0.900
4	Dermis	0.4585	356.5	0.900
5	Epidermis	16.5724	375.9	0.900
6	Skull	0.1154	282.0	0.900
7	Gray matter	2.3057	181.6	0.900
8	White matter	2.3057	181.6	0.900
9	Standard Tissue	1.000	100.0	0.900

5.3 Monte Carlo modeling of a Gaussian Beams into Multi layered Tissue

5.3.1 General Characteristics of Gaussian Beams

The beam originating from the laser source can be represented by Gaussian beam. The optical intensity of Gaussian beam is represented as [48],

$$I(r,z) = I_0 \left[\frac{W_0}{W(z)}\right]^2 exp\left[-\frac{2r^2}{W^2(z)}\right] \qquad 5.1$$

In the above equation r and z are the radial and axial distance respectively. I_0 is the center beam intensity which is expressed in watt per cm^2, W_0 is the waist radius expressed in cm, and $W(z)$ is the width of Gaussian beam in the z direction. The Gaussian beam width can be expressed as [49]:

$$W(z) = W_0[1 + (\frac{z}{z_0})^2]^{1/2} \qquad 5.2$$

Where, z_0 is the Rayleigh range of the Gaussian beam.

5.3.2 Monte Carlo Sampling of a Gaussian Beam profile

We have discussed the general representation of Gaussian beam. Now, the total power contained in the Gaussian beam is given as:

$$P = \frac{1}{2}\, I_0 (\pi {W_0}^2) \qquad 5.3$$

When z is equal to zero, the beam width is minimum. At this plane, we get the beam waist W_0. Therefore, total intensity is given by:

$$I(r) = I_0\, exp \left[-\frac{2r^2}{{W_0}^2} \right] \qquad 5.4$$

Considering power is equal to unity, above equation is simplified as,

$$I(r) = \frac{2}{\pi {W_0}^2}\, exp \left[-\frac{2r^2}{{W_0}^2} \right] \qquad 5.5$$

The probability density function for Gaussian beam in the r direction is given as,

$$p(r) = \frac{2}{\pi {W_0}^2}\, exp \left[-\frac{2r^2}{{W_0}^2} \right] . 2\pi r \qquad 5.6$$

Above equation can be simplified as,

$$p(r) = \frac{4r}{{W_0}^2}\, exp \left[-\frac{2r^2}{{W_0}^2} \right] \qquad 5.7$$

From this, we can get the cumulative distribution function.

For this radius r is assigned random variable. So, the cumulative distribution function at r=r_l is given by:

$$F(r_l) = \int_0^{r_i} p(r)dr = \left[1 - \exp(\frac{-2{r_l}^2}{{W_0}^2}) \right] = \xi_l \qquad 5.8$$

It gives sampling function for the sampled radius,

$$F(r_l) = \int_0^{r_i} p(r)dr = \left[1 - \exp(\frac{-2{r_l}^2}{{W_0}^2}) \right] = \xi_l \qquad 5.9$$

In the above equation ξ is the random variable. The simplified equation is given as:

$$r_l = \frac{W_0}{\sqrt{2}} \sqrt{-\ln(\xi_l)} \qquad 5.10$$

Above equation leads to “sampling rule A”.

It is necessary to verify the probability density function and Gaussian beam profile. MATLAB is used for building the probability density function. The obtained results are given in Fig. 5.2 and Fig. 5.3.

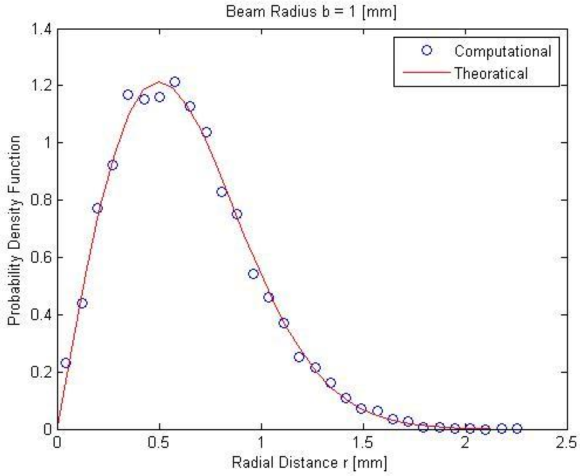

Figure 5.2: Probability density function of a Gaussian beam profile as per sampling rule A

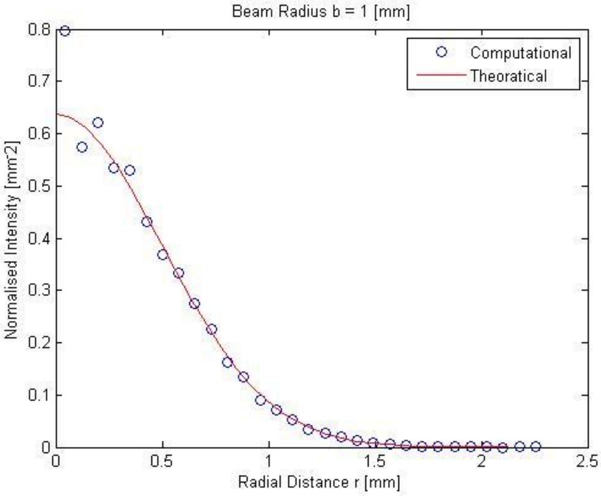

Figure 5.3: Normalized intensity profile of a Gaussian beam profile as per sampling rule A

While handling literature in depth, some references used another probability density function rather than one mentioned above. Another probability function is given below [50]:

$$p(r) = \frac{2r}{{W_b}^2} exp\left[-\frac{r^2}{{W_b}^2}\right] \qquad 5.11$$

In the above equation, W_b is the Gaussian beam radius also known as the Gaussian beam width. Now following the same steps as discussed earlier, the sampled radius is given as,

$$r_l = W_b\sqrt{-\ln(\xi_l)} \tag{5.12}$$

Above equation leads to "sampling rule B". We have given the names as sampling rule A and sampling rule B for the ease of comparison. By analyzing both, we can say that the definition of sampling beam width is not appropriate. The Gaussian beam width should be normalized by the square root of 2. The Monte Carlo simulations which depend on the sampling rule B gives an error. The relation between W_0 and W_b is given as,

$$W_b = \frac{W_0}{\sqrt{2}} \tag{5.13}$$

If we use sampling rule B, then it will give an error as it is not considering actual beam waist. For small beam waist W_0 the resulting error is small but in the case of large beam waist it increases further.

A plot for the probability density function and Gaussian beam profile by using sampling rule B is shown in Fig. 5.4 and Fig. 5.5.

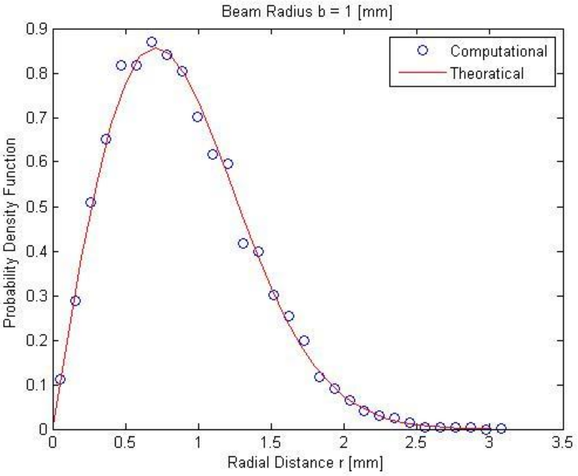

Figure 5.4: Probability density function of a Gaussian beam profile as per sampling rule B

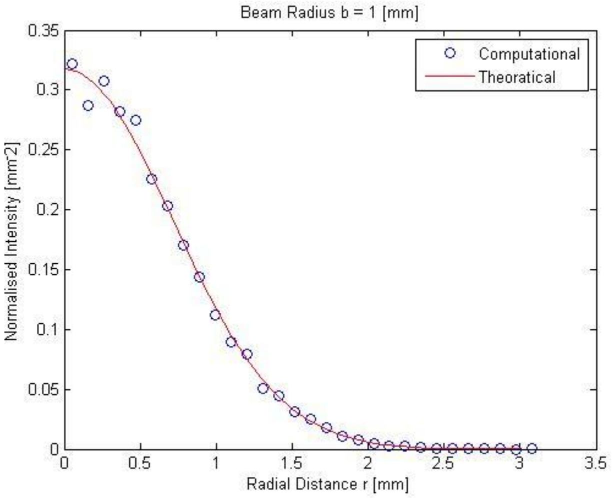

Figure 5.5: Normalized intensity profile of a Gaussian beam profile as per sampling rule B

There is a clear difference between width and height in Fig. 5.2 and Fig. 5.4. Same analysis suits for Gaussian intensity profiles as well. The Gaussian intensity profile shown in Figure 5.4 is the electric field and not the probability density function. The beam intensity approximately drops to $1/e$ instead of $1/e^2$.

Monte Carlo method is defined for probability density function and not for the electric field. So, the sampling rule B is not accurate for the use of Monte Carlo simulations for Gaussian Beam.

5.4 Monte Carlo Simulations of a different Gaussian Beam Profiles

5.4.1 Collimated Gaussian Beam

The probability density function of the radial position of launch is considered from the sampling rule B, which we have already discussed. The launching of a collimated Gaussian beam is given below.

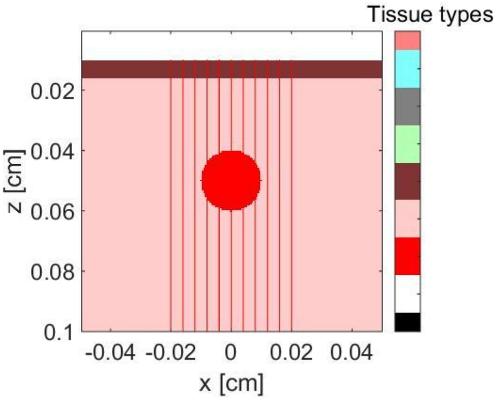

Figure 5.6: Collimated Gaussian beam for human skin

The absorption spectra of tissue due to collimated launch can be defined in terms of fluence rate after applying Monte Carlo approach to the skin tissue model. The fluence rate for collimated launch is given in Fig. 5.7.

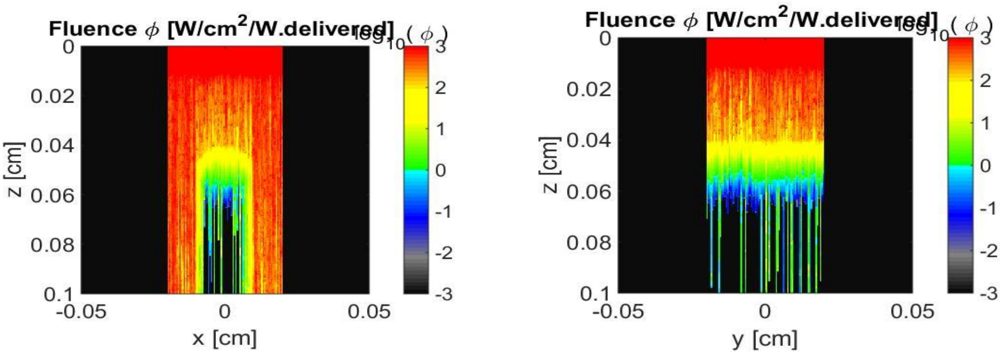

Figure 5.7: Fluence rate profile in ZX and ZY plane for collimated Gaussian beam

5.4.2 Focused Gaussian Beam

Similar analysis is also performed for focused Gaussian beam and same skin tissue model is used for the simulation of focused Gaussian beam.

So, the launching for beam is shown in Fig. 5.8.

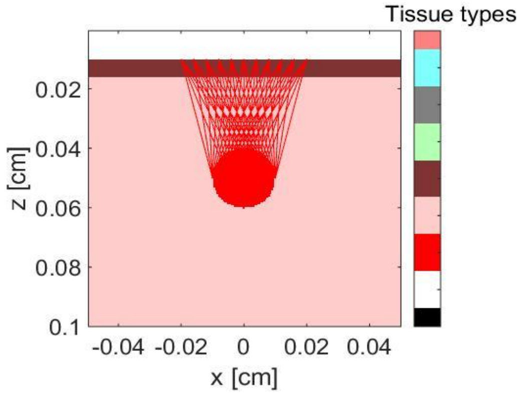

Figure 5.8 Focused Gaussian beam for human skin

Now, the absorption spectra is calculated in terms of fluence rate. The fluence rate for human skin after applying the focused Gaussian beam is shown in Fig. 5.9.

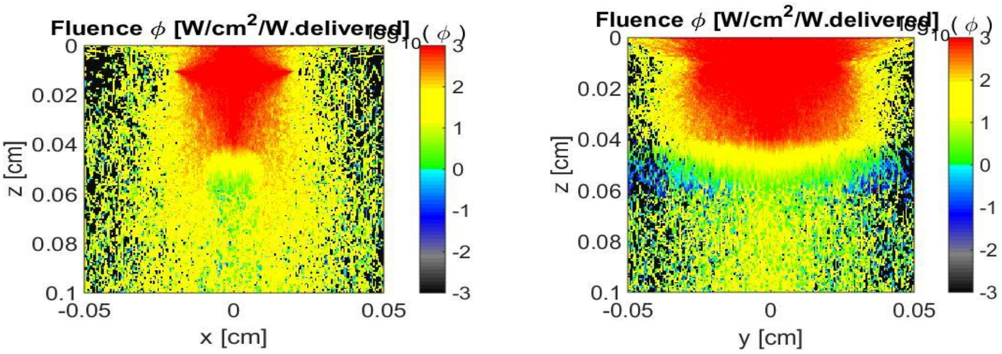

Figure 5.9 Fluence rate profile in ZX and ZY plane for focused Gaussian beam

5.5 Comparison of beam profiles at different beam radii

Simulation of different beam profiles is also done by using Multi Layered model of Monte Carlo. Monte Carlo analysis has been done at different radii for this beam profiles. The simulation spectra are shown in Fig. 5.10.

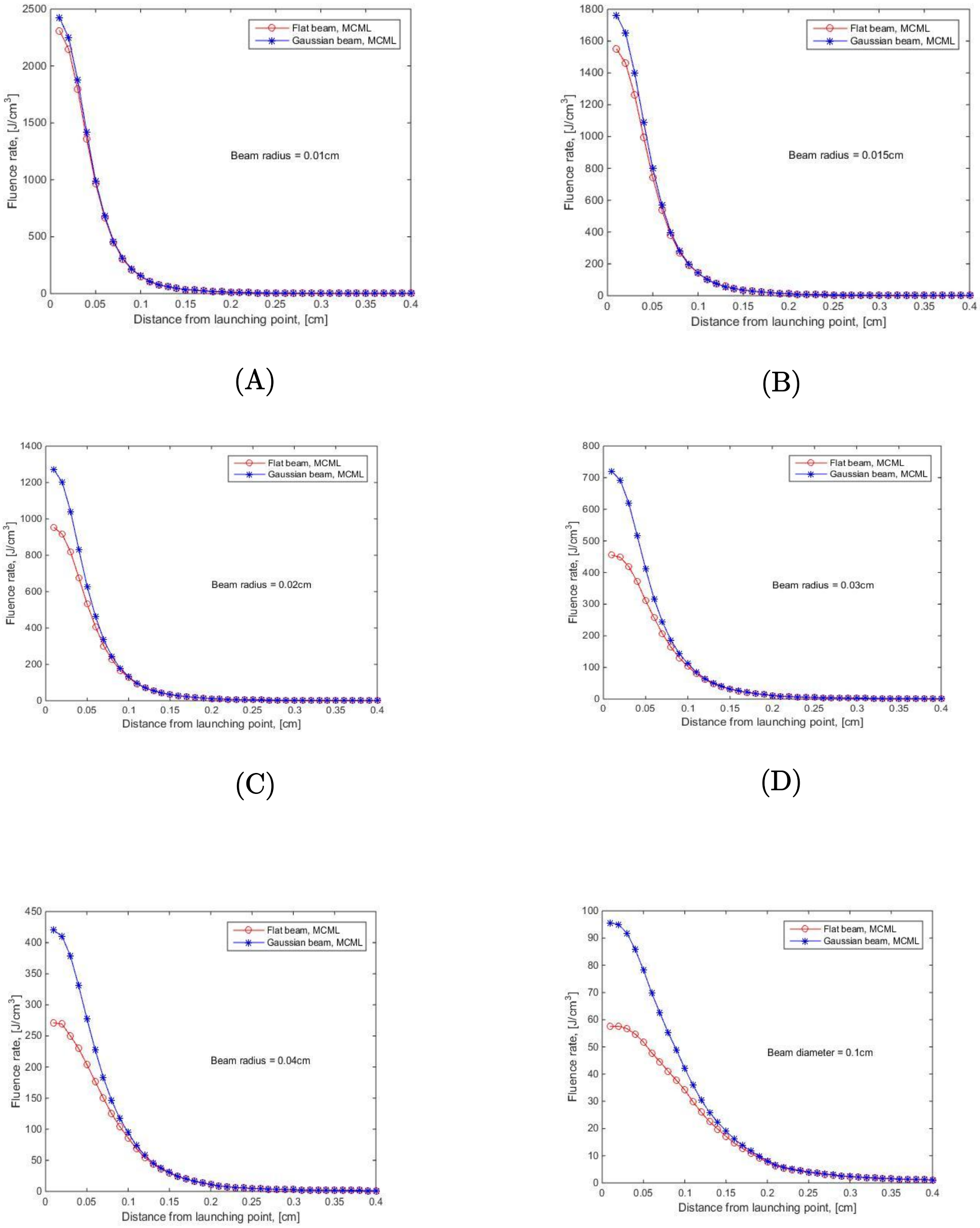

(A)

(B)

(C)

(D)

(E)

(F)

Figure 5.10: Similarities of fluence rate between flat-field beam and Gaussian beam is increasing as the beam size decreases

From this simulation we can conclude that as we change the beam radius there is decrease in the fluence spectra for both the profiles. Fluence rate decreases rapidly in flat field beam as compared to the Gaussian beam with the change in the beam radius. So, similarities of fluence rate between flat-field and Gaussian beam is decreasing as the beam size increases and vice versa.

Chapter 6

Summary and future work

In this thesis, the experimental setup for FF-OCT is developed. Reconstruction of FF-OCT is done by using phase stepping algorithm. For adding phase various methods are analyzed and proposed for the current setup. Future work can be aimed at applying proposed phase stepping techniques experimentally on the current FF-OCT setup. Optical source can be replaced to achieve much better resolution.

Mathematical modeling of human tissue is done by using Monte Carlo algorithm and different beam profiles are simulated on the skin tissue model. The sampling rule for the Gaussian beam has also been analyzed. Multi layered Monte Carlo model is considered for analysis of beam radius by varying the beam type. Monte Carlo simulations can be done for multiple human tissues. Future work can be aimed at the experimental verification on real biological tissues. Also, there is a need for mathematical modeling for other beam sources like Bessel beam and proper mathematical model should be developed for understanding new intensity profiles to avoid errors in simulation.

References

[1] D. Huang, E. A. Swanson, C. P. Lin, J. S. Schuman, W. G. Stinson, W. Chang, M. R. Hee, T. Flotte, K. Gregory, C. A. Puliafito, and al. et, "Optical coherence tomography.," *Science*, vol. 254, no. 5035, pp. 1178–81, Nov. 1991.

[2] M. R. Hee, J. A. Izatt, E. A. Swanson, D. Huang, J. S. Schuman, C. P. Lin, C. A. Puliafito, and J. G. Fujimoto, "Optical Coherence Tomography of the Human Retina," *Arch. Ophthalmol.*, vol. 113, no. 3, p. 325, Mar. 1995.

[3] E. J. Fernández, B. Považay, B. Hermann, A. Unterhuber, H. Sattmann, P. M. Prieto, R. Leitgeb, P. Ahnelt, P. Artal, and W. Drexler, "Three-dimensional adaptive optics ultrahigh-resolution optical coherence tomography using a liquid crystal spatial light modulator," *Vision Res.*, vol. 45, no. 28, pp. 3432–3444, 2005.

[4] J. Zhang, B. Rao, and Z. Chen, "Swept source based fourier domain functional optical coherence tomography," *Conf Proc IEEE Eng Med Biol Soc*, vol. 7, pp. 7230–7233, 2005.

[5] W. Drexler, U. Morgner, R. K. Ghanta, F. X. Kärtner, J. S. Schuman, and J. G. Fujimoto, "Ultrahigh-resolution ophthalmic optical coherence tomography.," *Nat. Med.*, vol. 7, no. 4, pp. 502–7, Apr. 2001.

[6] W. Drexler and J. G. Fujimoto, Eds., *Optical Coherence Tomography*. Berlin, Heidelberg: Springer Berlin Heidelberg, 2008.

[7] R. Leitgeb, C. Hitzenberger, and A. Fercher, "Performance of fourier domain vs time domain optical coherence tomography," *Opt. Express*, vol. 11, no. 8, p. 889, 2003.

[8] S. Chang, X. Liu, X. Cai, and C. P. Grover, "Full-field optical coherence tomography and its application to multiple-layer 2D information retrieving,"

Opt. Commun., vol. 246, no. 4–6, pp. 579–585, 2005.

[9] J. G. Fujimoto, M. E. Brezinski, G. J. Tearney, S. A. Boppart, B. Bouma, M. R. Hee, J. F. Southern, and E. A. Swanson, "Optical biopsy and imaging using optical coherence tomography," *Nat. Med.*, vol. 1, no. 9, pp. 970–972, Sep. 1995.

[10] G. J. Tearney, M. E. Brezinski, J. F. Southern, B. E. Bouma, S. A. Boppart, and J. G. Fujimoto, "Optical Biopsy in Human Urologic Tissue Using Optical Coherence Tomography," *J. Urol.*, vol. 157, no. 5, pp. 1915–1919, 1997.

[11] J. A. Izatt, M. D. Kulkarni, H.-W. Hsing-Wen Wang, K. Kobayashi, and M. V. Sivak, "Optical coherence tomography and microscopy in gastrointestinal tissues," *IEEE J. Sel. Top. Quantum Electron.*, vol. 2, no. 4, pp. 1017–1028, 1996.

[12] M. E. Brezinski, G. J. Tearney, S. A. Boppart, E. A. Swanson, J. F. Southern, and J. G. Fujimoto, "Optical Biopsy with Optical Coherence Tomography: Feasibility for Surgical Diagnostics," *J. Surg. Res.*, vol. 71, no. 1, pp. 32–40, 1997.

[13] S. A. Boppart, J. Herrmann, C. Pitris, D. L. Stamper, M. E. Brezinski, and J. G. Fujimoto, "High-Resolution Optical Coherence Tomography-Guided Laser Ablation of Surgical Tissue," *J. Surg. Res.*, vol. 82, no. 2, pp. 275–284, 1999.

[14] T. Anna, V. Srivastava, D. S. Mehta, and C. Shakher, "High-resolution full-field optical coherence microscopy using a Mirau interferometer for the quantitative imaging of biological cells," *Appl. Opt.*, vol. 50, no. 34, p. 6343, 2011.

[15] S. K. Dubey, G. Sheoran, T. Anna, A. Anand, D. S. Mehta, and C. Shakher, "Full-field swept-source optical coherence tomography with Gaussian spectral shaping," *Proc. SPIE*, vol. 7155, no. OCTOBER, p. 71551F–71551F–8, 2008.

[16] H. M. Subhash, "Full-field and single-shot full-field optical coherence tomography: A novel technique for biomedical imaging applications," *Adv.*

Opt. Technol., vol. 2012, 2012.

[17] K. Grieve, A. Dubois, M. Simonutti, M. Paques, J. Sahel, J.-F. Le Gargasson, and C. Boccara, “In vivo anterior segment imaging in the rat eye with high speed white light full-field optical coherence tomography,” *Opt. Express*, vol. 13, no. 16, p. 6286, 2005.

[18] A. Dubois, “Extended full-field optical coherence microscopy,” *Sel. Top. Opt. Coherence Tomogr.*, no. May, 2012.

[19] Scott Prahl, “Optical Absorption of Water,” 1998. [Online]. Available: http://omlc.org/spectra/water/. [Accessed: 05-Mar-2015].

[20] T. Anna, C. Shakher, and D. S. Mehta, “Three-dimensional shape measurement of micro-lens arrays using full-field swept-source optical coherence tomography,” *Opt. Lasers Eng.*, vol. 48, no. 11, pp. 1145–1151, 2010.

[21] S. K. Dubey, T. Anna, C. Shakher, and D. S. Mehta, “Fingerprint detection using full-field swept-source optical coherence tomography,” *Appl. Phys. Lett.*, vol. 91, no. 18, pp. 1–4, 2007.

[22] V. Srivastava, T. Anna, M. Sudan, and D. S. Mehta, “Tomographic and volumetric reconstruction of composite materials using full-field swept-source optical coherence tomography,” *Meas. Sci. Technol.*, vol. 23, no. 5, p. 055203, 2012.

[23] Y. Zhu and W. Gao, “High-resolution imaging of biological tissue with full-field optical coherence tomography,” *SPIE BiOS*, no. JANUARY 2015, p. 93301H, 2015.

[24] S. Chang, X. Cai, and C. Flueraru, “An efficient algorithm used for full-field optical coherence tomography,” *Opt. Lasers Eng.*, vol. 45, no. 12, pp. 1170–1176, 2007.

[25] C. W. Lee, “General methods for L / M -fold resizing of compressed images using lapped transforms,” *IET Image Process.*, vol. 1, no. 3, pp. 295–303, 2007.

[26] M. J. C. Van Gemert, S. L. Jacques, H. J. C. M. Sterenborg, and W. M. Star, “Skin optics,” *IEEE Trans. Biomed. Eng.*, vol. 36, no. 12, pp. 1146–1154, 1989.

[27] S. T. Flock, S. L. Jacques, B. C. Wilson, W. M. Star, and M. J. C. van Gemert, “Optical properties of intralipid: A phantom medium for light propagation studies,” *Lasers Surg. Med.*, vol. 12, no. 5, pp. 510–519, 1992.

[28] J. Henniger, O. Minet, H. T. Dang, and J. Beuthan, “Monte Carlo Simulations in Complex Geometries : Modeling Laser Light Transport in Real Anatomy of Rheumatoid Arthritis,” vol. 13, no. 5, pp. 796–803, 2003.

[29] S. L. Jacques, “Monte Carlo Modeling of Light Transport in Tissue (Steady State and Time of Flight),” in *Optical-Thermal Response of Laser-Irradiated Tissue*, Dordrecht: Springer Netherlands, 2010, pp. 109–144.

[30] V. V. Tuchin, A. N. Yaroslavsky, S. L. Jacques, and R. Anderson, “Biophotonics for dermatology: science &amp; applications,” *J. Biophotonics*, vol. 3, no. 1–2, pp. 9–10, Dec. 2009.

[31] V. M. Rossi, S. B. Gustafson, and S. L. Jacques, “Characterizing the Optical Properties of Bone Using a Multi-Fiber Array and Diffuse Reflectance Spectroscopy,” in *Frontiers in Optics 2009/Laser Science XXV/Fall 2009 OSA Optics & Photonics Technical Digest*, 2009, p. FME4.

[32] S. L. Jacques, “Modeling tissue optics using Monte Carlo modeling: a tutorial,” 2008, p. 68540T–68540T–9.

[33] W. F. Cheong, S. a. S. Prahl, and a. J. A. Welch, “A review of the optical properties of biological tissues,” *IEEE journal of quantum electronics*, vol. 26, no. 12. pp. 2166–2185, 1990.

[34] S. A. Prahl, M. Keijzer, S. L. Jacques, and A. J. Welch, “A Monte Carlo Model of Light Propagation in Tissue.”

[35] S. P. Steven Jacques, “Absorption spectra for biological tissues,” 1998. [Online]. Available: http://omlc.org/classroom/ece532/class3/muaspectra.html. [Accessed: 05-

Mar-2015].

[36] S. P. Steven Jacques, “Definition of anisotroppy,” 1998. [Online]. Available: http://omlc.org/classroom/ece532/class3/gdefinition.html. [Accessed: 05-Mar-2015].

[37] S. L. J. and L.-H. Wang, “Monte Carlo modeling of light transport in tissues,” *Opt. Therm. Response Laser Irradiat. Tissue*, vol. 2607, no. 713, pp. 73 – 100, 1995.

[38] L. Wang and S. L. Jacques, “Monte Carlo Modeling of Light Transport in Multi-layered Tissues in Standard C Monte Carlo Modeling of Light Transport in Multi-layered Tissues in Standard C,” p. 173, 1992.

[39] L. Wang, S. L. Jacques, and L. Zheng, “Conv—convolution for responses to a finite diameter photon beam incident on multi-layered tissues,” *Comput. Methods Programs Biomed.*, vol. 54, no. 3, pp. 141–150, 1997.

[40] D. Gareau, S. Jacques, and J. Krueger, “Monte Carlo modeling of pigmented lesions,” 2014, p. 89260V.

[41] M. Carlo, “The Henyey-Greenstein phase function .,” *PoLAR*, pp. 1–6, 1941.

[42] K. Kamiuto, “Study of the Henyey-Greenstein approximation to scattering phase functions,” *J. Quant. Spectrosc. Radiat. Transf.*, vol. 37, no. 4, pp. 411–413, 1987.

[43] G. C. Pomraning, “On the Henyey-Greenstein approximation to scattering phase functions,” *J. Quant. Spectrosc. Radiat. Transf.*, vol. 39, no. 2, pp. 109–113, Feb. 1988.

[44] B. Jeeva and M. Singh, “Detection of tumour in biological tissues by laser backscattering and transillumination signal analysis,” *Curr. Sci.*, vol. 107, no. 11, pp. 1824–1831, 2014.

[45] S. Chen, S. Member, J. Yi, W. Liu, S. Member, and V. Backman, “Monte Carlo Investigation of Optical Coherence Tomography Retinal Oximetry,” vol. 9294, no. c, 2015.

[46] R. Alcouffe, R. Dautray, A. Forster, G. Ledanois, and B. Mercier, Eds.,

Monte-Carlo Methods and Applications in Neutronics, Photonics and Statistical Physics, vol. 240. Berlin/Heidelberg: Springer-Verlag, 1985.

[47] J. S. Hendricks and T. E. Booth, “MCNP variance reduction overview,” in *Monte-Carlo Methods and Applications in Neutronics, Photonics and Statistical Physics*, Berlin/Heidelberg: Springer-Verlag, 1985, pp. 83–92.

[48] B. E. A. Saleh and M. C. Teich, *Fundamentals of photonics*. Wiley-Interscience, 2007.

[49] I. S. A. El Ghargomi, “Modeling of Focused Gaussian Beam into Multi-Layered Tissue with Monte Carlo Simulation,” 2004.

[50] A. Tycho, T. M. Jørgensen, H. T. Yura, and P. E. Andersen, “Derivation of a Monte Carlo method for modeling heterodyne detection in optical coherence tomography systems,” *Appl. Opt.*, vol. 41, no. 31, p. 6676, Nov. 2002.